



SUPER-RESOLUTION SURFACE RECONSTRUCTION FROM FEW LOW-RESOLUTION SLICES

YIYAO ZHANG^{✉1,2} AND KE CHEN^{✉*3} AND SHANG-HUA YANG^{✉2}

¹ Centre for Mathematical Imaging Techniques and Department of Mathematical Sciences
University of Liverpool, Liverpool, United Kingdom (UK)

² Institute of Electronics Engineering, Department of Electrical Engineering
National Tsing Hua University, Taiwan

³ Department of Mathematics and Statistics, University of Strathclyde, Glasgow, UK and
Centre for Mathematical Imaging Techniques, University of Liverpool, Liverpool, UK

(Communicated by Handling Editor)

ABSTRACT. In many imaging applications where segmented features (e.g. blood vessels) are further used for other numerical simulations (e.g. finite element analysis), the obtained surfaces do not have fine resolutions suitable for the task. Increasing the resolution of such surfaces becomes crucial. This paper proposes a new variational model for solving this problem, based on an Euler-Elastica-based regulariser. Further, we propose and implement two numerical algorithms for solving the model, a projected gradient descent method and the alternating direction method of multipliers. Numerical experiments using real-life examples (including two from outputs of another variational model) have been illustrated for effectiveness. The advantages of the new model are shown through quantitative comparisons by the standard deviation of Gaussian curvatures and mean curvatures from the viewpoint of discrete geometry.

1. Introduction. In this paper, we propose a new variational model for getting a faster and smoother three-dimensional (3D) surface reconstruction in high resolution from the collection of a few low-resolution images (input of cross-sections or slices), where the gaps of given slices are often large and uneven. There are various practical or operational reasons why only low-resolution data (often with poor quality by way of artefacts or noise) are available. For example, imaging equipment may have limitations, such as short scanning times or low radiation doses to minimise harm or damage to patients. A more subtle reason is that the region of interest (RoI) may be very small in a large and high-resolution (HR) image. Hence, it is necessary to develop appropriate and suitable mathematical models to reconstruct HR surfaces as far as the RoI is concerned. Once a HR datum (surface) is achieved, further measures or even new simulations based on the new geometry can be conducted, such as finite element analysis of blood flows in clinical imaging. Though the surface reconstruction problem arises as a problem in discrete geometry (see Figure 1), we shall develop a variational model for solving it.

2020 *Mathematics Subject Classification.* Primary: 49Q20, 65K10, 65D18, 94A08; Secondary: 68U10.

Key words and phrases. Surface reconstruction, Variational model, perimeter energy, Willmore energy, Euler-Elastica energy, Phase-field approximation, Γ -convergence, Alternating direction method of multipliers, Gaussian curvature, Mean curvature, Discrete geometry.

The first author is partially supported by the UoL-NTHU Dual PhD Programme.

*Corresponding author: Ke Chen (K.Chen@strath.ac.uk) [www.liv.ac.uk/~cmchenke].



Figure 1. Three-dimensional reconstruction of Branching Cylinder by the new proposed Euler-Elastica-based model from low-resolution inputs $N = 128$ with 24 deliberately uneven slices.

The problem under study might be classified as an inpainting problem in which gaps are filled in some manner [15]. Mathematical methods using variational models based on partial-differential-equation-based (PDE-based) have been widely exploited in image processing since the 1990s, as these approaches can accurately simulate our real, visible and physical world as evident from diverse application areas such as medicine, economics, and computer vision [16, 17]. Beyond imaging processing, the topic of 3D surface inpainting is much less studied in the variational framework.

In discrete geometry, many works exist for surface reconstruction. For retrieving the 3D shape, mathematical methods can be roughly divided into two categories depending on the surface representations: (i) the explicit reconstruction (e.g. Delaunay triangulation [18], and Voronoi diagram [25, 1, 24]), and (ii) the implicit reconstruction (e.g. radial basis functions [27], Poisson reconstruction [29, 8], and level set method [3, 28, 13]). In a nutshell, surfaces by category (i) are typically piecewise linear and these methods are relatively easy to implement. Although this kind of representation is suitable for graphics purposes, it is tough to cope with the non-uniform or potentially noisy or incomplete data e.g. if vertices and faces of the surface are not sufficient, and also have difficulties in tracking the topological changes and large deformations. Category (ii) methods can produce reconstructions through forming a physical model based on differentiable distance functions over an implicit surface and are capable of coping better with the cases of non-uniform or potentially noisy or incomplete data.

This paper proposes a method in category (ii) inspired by the lucid reconstructed framework delineated by Bretin, Dayrens, and Masnou [3] by applying geometric variational energies with the phase-field approximation, which are more pleasant to work with numerically than category (i) methods. Two regularisation energies (perimeter-based energy and Willmore-based energy) were applied in the framework by [3]. Connecting with the phase-field approximation, the perimeter-based formulation (Van der Waals-Cahn-Hilliard energy) and the Willmore-based formulation are reformulated where the linear obstacle slack restrictions are constituted by the low-resolution input slices as the shape constraint. Nevertheless, there are some defects for these two proposed formulations as Figures 2-3 show.

Figure 2 shows the final reconstruction result using the perimeter-based formulation, and it does not fully satisfy our visual criteria globally. Although it successfully preserves edge features, particularly on the flat tops of the input slices, due to its energy being connected with the total variation, the overall result still contains defects with jagged edges and other undesirable artefacts. On the other hand, Figure 3 displays the result using the Willmore-based formulation, which has fewer defects compared to the perimeter-based formulation, resulting in smoother and more natural surfaces. However, it tends to plump up the top plane due to the close relationship of Willmore energy with mean curvature, and there may be bumps if the number of input slices is not sufficiently large in the given lower resolution. As such, the challenge becomes how to obtain a suitable variational model beyond the energy using mean curvature regularisation that can better address these issues.

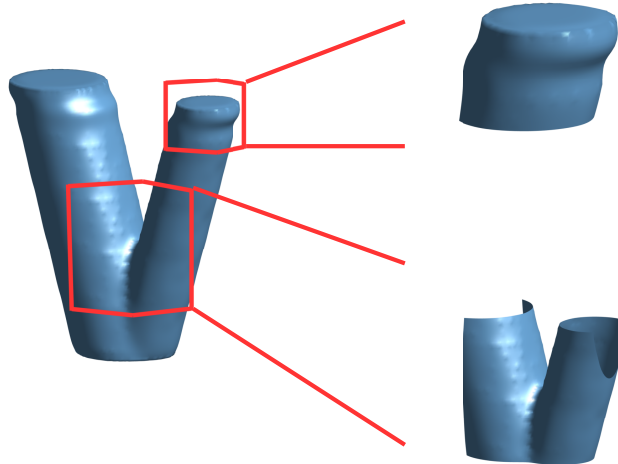


Figure 2. Reconstruction results with defects (top right: flattened top with jagged edges and sunken shape; bottom: serious bumps) by the perimeter-based formulation of Branching Cylinders from low-resolution inputs $N = 128$ with 24 uneven collected input slices (the left-hand side of Figure 1).

Therefore, to improve on [3], we must employ some geometric regulariser that outperforms the mean curvature. Motivated by other image processing works [4, 10] where the Euler-Elastica-based formulations are better than the formulation related to mean curvature, our proposed work overcomes above deficiencies by minimising the Euler-Elastica-based energy. Apart from the question of how to solve the new formulation, an interesting problem arises in comparing different models: how to deal with the different or inconsistent numbers of triangular meshes for final surfaces for a fair and objective comparison of results by different formulations? We address this by computing the standard deviation of Gaussian curvatures (GC) and mean curvatures (MC) to indicate the corresponding level of smoothness from the viewpoint of discrete geometry, which is stimulated by [20, 21].

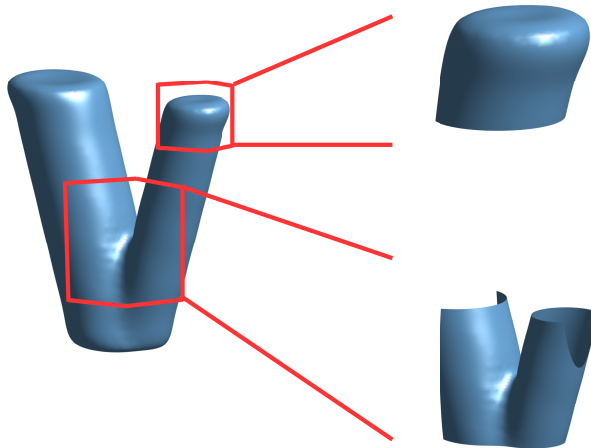
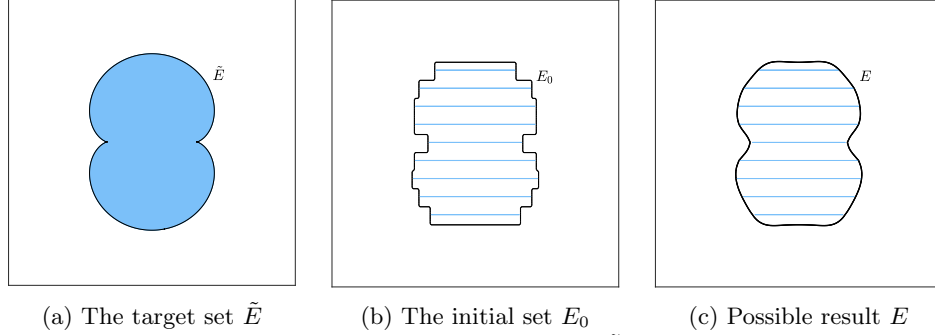


Figure 3. Reconstruction results with defects (top right: bulging top with dented centre and jagged edges slightly; bottom: slight bumps) by the Willmore-based formulation of Branching Cylinders from low-resolution inputs $N = 128$ with 24 uneven collected input slices (the left-hand side of Figure 1).

The rest of this paper is organised as follows: Section 2 introduces some essential mathematical preliminaries, including definitions and notations for the reconstructed framework of a geometric variational method, linear obstacle slack restrictions, and phase-field approximation. Section 3 proposes the new Euler-Elastica-based formulation first and derives the Euler-Lagrange equation, and then presents two numerical algorithms for solving the resulting optimisation problem where we extend the alternating direction method of multipliers (ADMM) to solve our model, which leads to faster numerical approximations. Finally, simulated and realistic examples are depicted and compared in Section 4 by different models (inpainting models and three formulations), where quantitative comparisons are also given to show the effectiveness of the new Euler-Elastica-based formulation.

2. Mathematical Preliminaries. The goal is to obtain a smooth D -dimensional reconstruction $E^* \subset \mathbb{R}^D$ from the initial set E_0 , as Figure 4 exemplified, where \tilde{E} is the desired target set and E denotes as the possible reconstruction. Here the initial set E_0 consists of given parallel cross-sections $\Pi_s \subset \mathbb{R}^D$ with the number of slices $s \in \mathbb{N}^*$. We provide visual illustrations using the two-dimensional scenario ($D = 2$ for curve smoothing) to clarify some of the notations in this section (significant notations are summarised in Appendix A). The primary implementations for the three-dimensional scenario ($D = 3$ for surface reconstruction) are presented in Section 4. In this section, we first introduce a shape-preserving approach by interior and exterior restrictions to maintain the shape of the input set during reconstruction. Later, we address the challenge of formulating and computing variational energies by employing a phase-field method. This approach allows us to represent the variational energies using a smooth and continuous function, which can be easily discretised and optimised numerically.



(a) The target set \tilde{E} (b) The initial set E_0 (c) Possible result E

Figure 4. Exemplification of the target set \tilde{E} (left), the initial set E_0 (centre) and the possible construction E (right) in the two-dimensional scenario.

2.1. Fidelity by Interior and Exterior Restrictions. To address the challenge of incorporating restrictions based on the initial set E_0 using a collection of s finite hyperplanes $\{\Pi_s\}$, we adopt a fidelity-driven approach to the reconstruction process. It is worth noting that for any two distinct hyperplanes $s_1 \neq s_2$, we assume that $\Pi_{s_1} \cap \Pi_{s_2} = \emptyset$, and hyperplanes can be expressed as $\Pi_s = \{(\xi, 0) : \xi \in \mathbb{R}^{D-1}\}$ if an appropriate orthonormal system of coordinates is chosen in \mathbb{R}^D (this is possible due to slices being parallel and sitting in a low dimension). To preserve the shape of the input data, we use a term in this approach similar to the fidelity term used in other variational models. However, due to the discrete nature of the input data in E_0 , we do not strictly use the least-squares fidelity term, such as $\int_{\Omega} |E^* - E_0|^2 d\Omega$, in the following setting. Specifically, we first introduce interior and exterior restrictions $\omega^{in} := \omega_{E_0}^{in}$ and $\omega^{ex} := \omega_{E_0}^{ex}$ respectively, which are originated from the set of hyperplanes related to the initial set E_0

$$\omega^{in} := \omega_{E_0}^{in} = \bigcup_s \omega_s^{in} \quad \text{and} \quad \omega^{ex} := \omega_{E_0}^{ex} = \bigcup_s \omega_s^{ex}$$

where $\omega_s^{in}, \omega_s^{ex}$ are preset based on Π_s . Here,

- $\omega_s^{in}, \omega_s^{ex} \subset \{\Pi_s\}$ as Figure 5(a) illustrated, i.e. $\omega_s^{in}, \omega_s^{ex} \subset \Pi_s$,
- $\omega_s^{in} \subset E_0 \cap \Pi_s \subset \Pi_s \setminus \omega_s^{ex}$ satisfies for every initial object E_0 , and
- $\omega_s^{in} \cup \omega_s^{ex} \supset \Pi_s$ does not require as it enables to handle noisy inputs.

Then, the problem for reconstruction from slices can be formulated as a variational model, which is to find the (local) minimum E^* subject to

$$E^* = \underset{\substack{\omega^{in} \subset E \\ E \cap \omega^{ex} = \emptyset}}{\text{argmin}} \mathcal{E}(E) \quad (1)$$

where ω^{in}, ω^{ex} are interior and exterior restrictions from the initial set E_0 , and \mathcal{E} can be the perimeter-based \mathcal{P} , the Willmore-based \mathcal{W} , and the Euler-Elastica-based \mathcal{E} energy, as shown shortly in Section 2.2 to impose smoothness on the surface ∂E .

Next, we suggest two fattened restrictions depicted in Figure 5(b) to enhance more flexibility during the reconstruction process. As we only have a limited number of slices, these restrictions are designed to enlarge the feasible region and improve the reconstruction. Define the fattened interior and exterior restrictions as follows:

$$\Omega^{in} := \Omega_{E_0}^{in} = \bigcup_s \Omega_{s,h}^{in} \quad \text{and} \quad \Omega^{ex} := \Omega_{E_0}^{ex} = \bigcup_s \Omega_{s,h}^{ex}$$

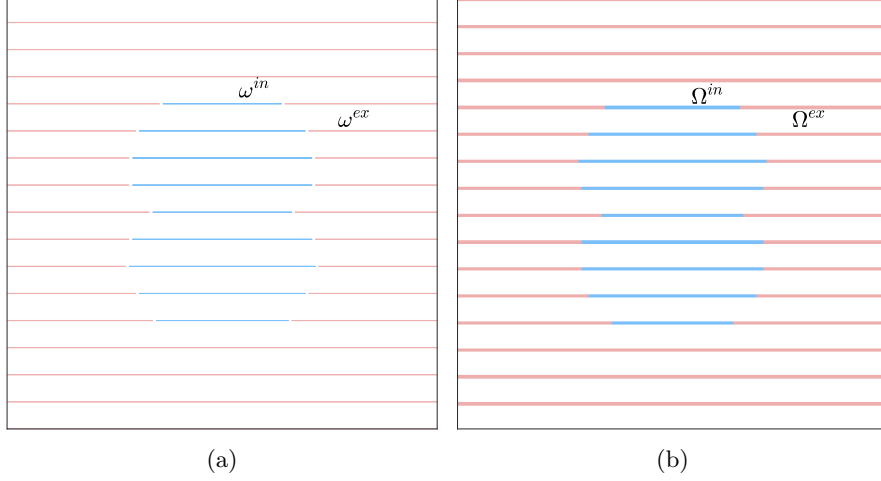


Figure 5. Illustrations of (a) interior restrictions ω^{in} (cyan) and exterior restrictions ω^{ex} (pink), and of (b) fattened interior restrictions Ω^{in} (cyan) and exterior restrictions Ω^{ex} (pink) from the initial set E_0 .

where the thickness parameter $h = \varepsilon^\alpha > 0$ is determined by given $\varepsilon > 0$ and $\alpha \in [0, 1]$. Here, h controls the thickness of the restrictions, and the value of α determines the rate at which the thickness increases with ε . To define $\Omega_{s,h}^{in}$ and $\Omega_{s,h}^{ex}$, we use the signed distance function (or called oriented distance function) d_s to an arbitrary subset π_s of hyperplanes Π_s . The restrictions are then defined as:

$$\begin{aligned}\Omega_{s,h}^{in} &= \{(\xi, \zeta) \in (\mathbb{R}^{D-1} \times \mathbb{R}) \cap E_0 : \xi \in \omega_s^{in}, |\zeta| < h|d_s(\xi, \omega_s^{in})|\}, \\ \Omega_{s,h}^{ex} &= \{(\xi, \zeta) \in (\mathbb{R}^{D-1} \times \mathbb{R}) \cap E_0 : \xi \in \omega_s^{ex}, |\zeta| < h|d_s(\xi, \omega_s^{ex})|\},\end{aligned}$$

as Figure 6 illustrated where they are fixed from initial set E_0 . Here, the signed distance function d_s is given by $d_s(\xi, \pi_s) = \text{dist}(\xi, \pi_s) - \text{dist}(\xi, \Pi_s \setminus \pi_s)$ for arbitrary $\xi \in \Pi_s$ and $\pi_s \subset \Pi_s$ where $\text{dist}(\cdot, \cdot)$ is the representative Euclidean distance in \mathbb{R}^D [14].

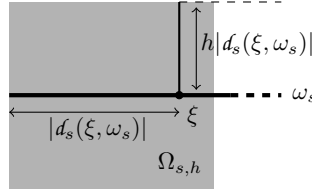


Figure 6. Illustration of the fattened restriction of ω_s with the thickness parameter h where part of the fattened region $\Omega_{s,h} = \{(\xi, \zeta) \in (\mathbb{R}^{D-1} \times \mathbb{R}) \cap E_0 : \xi \in \omega_s, |\zeta| < h|d_s(\xi, \omega_s)|\}$ is shown in gray.

Therefore, incorporating the fattened restrictions, model (1) becomes

$$E^* = \underset{\substack{\Omega^{in} \subset E \\ E \cap \Omega^{ex} = \emptyset}}{\text{argmin}} \mathcal{E}(E) \quad (2)$$

where fattened restrictions Ω^{in}, Ω^{ex} are defined from E_0 , and \mathcal{E} as a general the energy function can be $\mathcal{P}, \mathcal{W}, \mathcal{E}$ (to be introduced shortly in Section 2.2).

2.2. Relaxation by Phase-field Approximation. The difficulty with model (2) is that the unknown is the set E , not a function representing E . We now introduce the phase-field method to represent the set by a function, and then turn the problem into a variational problem before considering discretisation and numerical solution. The phase-field method is a widely used technique for modelling complex physical phenomena with sharp interfaces or discontinuities, such as phase transitions, fracture, and grain growth, among others. In essence, the phase-field method replaces the sharp interface or discontinuity with a diffuse interface or transition zone of finite thickness, which is controlled by a scalar parameter known as the phase-field variable. By doing so, the problem becomes amenable to standard numerical methods for solving partial differential equations, such as finite differences, finite elements, or spectral methods, among others. In the following, we will describe how to use the phase-field method to approximate the binary indicator function and reformulate the inverse problem (2) involving the phase-field approximation.

In order to describe the representation of the set E by the phase-field function (recall that E_0 is the initial set and E is the possible solution), Modica and Mortola in [9], as well as Bretin, Dayrens, and Masnou in [3, 26] have proposed a sequence (u_ε) (i.e. phase-field function $u_\varepsilon(\cdot)$) defined as follows

$$u_\varepsilon(\xi) = q\left(\frac{d(\xi, E)}{\varepsilon}\right). \quad (3)$$

This sequence is used to approximate the indicator function of set E that characterises the interface between the target object and background region. Here,

- $d(\xi, E)$ is the signed distance function that measures the distance between the given point ξ and the boundary ∂E of the set E . Specifically,

$$d(\xi, E) \begin{cases} < 0 & \text{when } \xi \in E \setminus \partial E \\ = 0 & \text{when } \xi \in \partial E \\ > 0 & \text{otherwise} \end{cases},$$

as Figure 7(a) shows. Note that $|d(\xi, E)|$ gives the shortest distance from ξ to the boundary ∂E with the property $|\nabla d| = 1$ [3, 26, 6].

- ε is the phase-field variable related to the thickness parameter $h = \varepsilon^\alpha$ as previously mentioned.
- q is called the profile function, which is required to be a piecewise function that takes the value of 1 inside E , half on ∂E , and 0 outside E and is designed to enforce the continuity and smoothness of the phase-field function.

Then, the phase-field approximation method provides an equivalence between fattened restrictions and phase-field functions by

$$\Omega^{in} \subset E \subset \mathbb{R}^D \setminus \Omega^{ex} \iff u_\varepsilon^{in} \leq u_\varepsilon \leq u_\varepsilon^{ex} \quad (4)$$

where the phase-field profiles $u_\varepsilon^{in}, u_\varepsilon^{ex}$ by (3) are defined by

$$u_\varepsilon^{in} = q\left(\frac{d(\xi, \Omega^{in})}{\varepsilon}\right) \quad \text{and} \quad u_\varepsilon^{ex} = 1 - q\left(\frac{d(\xi, \Omega^{ex})}{\varepsilon}\right), \quad (5)$$

and the latter of (4) is called linear obstacle restrictions on u_ε , which serves as an obstacle for the minimisation problem and allows the minimiser to satisfy the restrictions.

Next, to determine the profile function q that satisfied the above requirements of being 1 inside E , half on ∂E , and 0 outside E , one suggestion is to utilise the double-well potential W [3]. The Euler equation $q'' = W'(q)$ with the initial condition $q(0)$ can be solved as the following Cauchy problem for $W \in \mathbb{C}^2$

$$q' = -\sqrt{2W(q)} \quad \text{and} \quad q(0) = \frac{1}{2}.$$

For the specific case of the double-well potential given by $W(u) = \frac{1}{2}u^2(1-u)^2$, the profile function q can be deduced via the separation of variables as

$$q(\xi) = \frac{1}{2} \left(1 - \tanh \left(\frac{\xi}{2} \right) \right) = \frac{1}{1 + e^\xi}. \quad (6)$$

Then, by using the profile function q , the interior region Ω^{in} and exterior region Ω^{ex} of the initial object E_0 can be indicated as 1 and 0 respectively, and in fact, two phase-field profiles by (5) have the following convergence results

$$u_\varepsilon^{in}(\xi) \xrightarrow{\varepsilon \rightarrow 0} \begin{cases} 1 & \text{if } \xi \in \Omega^{in} \\ \frac{1}{2} & \text{if } \xi \in \partial\Omega^{in} \\ 0 & \text{otherwise} \end{cases} \quad \text{and} \quad u_\varepsilon^{ex}(\xi) \xrightarrow{\varepsilon \rightarrow 0} \begin{cases} 0 & \text{if } \xi \in \Omega^{ex} \\ \frac{1}{2} & \text{if } \xi \in \partial\Omega^{ex} \\ 1 & \text{otherwise} \end{cases} \quad (7)$$

as Figure 7(b) sketched. Furthermore, these profiles can be indicated by

$$u_\varepsilon^{in} = \frac{1}{2} \mathbb{1}_{\Omega^{in}} \quad \text{and} \quad u_\varepsilon^{ex} = 1 - \frac{1}{2} \mathbb{1}_{\Omega^{ex}}. \quad (8)$$

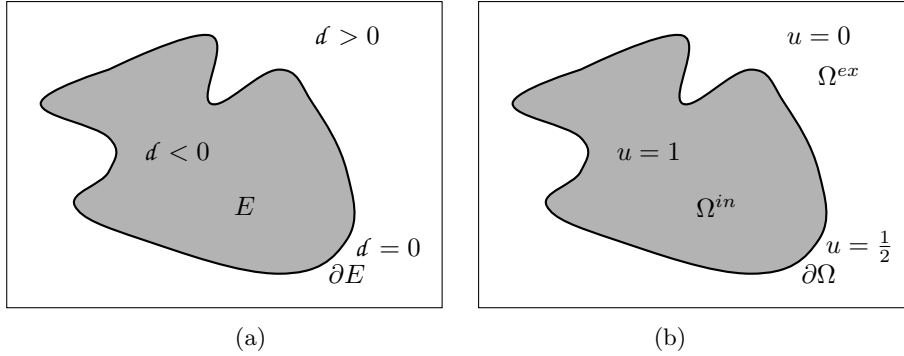


Figure 7. Illustrations of (a) the signed distance function (negative inside E , zero on the boundary, and positive outside), and of (b) the values of u for the interior region Ω^{in} , boundary $\partial\Omega$, and the exterior region Ω^{ex} of the object E using the profile function q .

Naturally, the variational framework (2) with the phase-field relaxation is reformulated as:

$$u_\varepsilon^* = \operatorname{argmin}_{u_{E_0}^{in} \leq u \leq u_{E_0}^{ex}} \mathcal{E}_\varepsilon(u), \quad (9)$$

where $u := u_\varepsilon, u_{E_0}^{in} := u_\varepsilon^{in}, u_{E_0}^{ex} := u_\varepsilon^{ex}$ after omitting ε for simplified, two restrictions are associated with the initial set E_0 , and \mathcal{E}_ε can be the perimeter-based \mathcal{P}_ε , Willmore-based \mathcal{W}_ε and Euler-Elastica-based \mathcal{E}_ε formulation from corresponding energies $\mathcal{E} = \mathcal{P}, \mathcal{W}, \mathcal{E}$, to be introduced in (10)-(12) for energies, and (13), (15), (16) for formulations.

Our framework incorporates three classical energies: the perimeter-based \mathcal{P} , the Willmore-based \mathcal{W} , and the Euler-Elastica-based \mathcal{E} energy [3, 10, 12, 11]. These energies with their properties have been extensively studied in image processing and are now extended to our surface reconstruction problem.

(\mathcal{P}) The perimeter-based energy is the first energy we consider, expressed as

$$\mathcal{P}(E) = \int_{\partial E} \mathbb{1}_E d\mathcal{H}^{D-1} \quad (10)$$

where $\mathbb{1}_E$ is alluded to the indicator function or the characteristic function of the set E that indicates elements in the set E [26, 7], that is, $\mathbb{1}_E(\xi) = 1$ if $\xi \in E$ and 0 otherwise, \mathcal{H}^{D-1} denotes the $(D-1)$ -dimensional Hausdorff measure in \mathbb{R}^D and ∂E is the boundary of E . The perimeter-based energy is a simple and intuitive way to measure the length or surface area of a given set. One of the key properties of this energy is that it is scale-invariant, meaning that it does not depend on the size or location of the set being measured. Additionally, it has a well-defined gradient that can be used for optimisation purposes. However, it can be sensitive to noise and can be affected by irregularities in the boundary of the set. Besides, there is a relationship between the perimeter energy and the total variation (TV) functional. In fact, the perimeter energy can be viewed as a special case of the TV functional, where the signal or image is a binary indicator function of a set. More generally, the TV functional can be seen as a generalisation of the perimeter energy to functions that are not binary indicator functions.

(\mathcal{W}) For the second choice of energy: Willmore-based energy is defined by

$$\mathcal{W}(E) = \int_{\partial E} |H|^2 d\mathcal{H}^{D-1} \quad (11)$$

where H is the mean curvature on the boundary ∂E . The Willmore energy is a geometric energy that measures the bending or deviation of a surface from a plane. This energy is quadratic in the mean curvature of the surface, which captures both its local and global curvature information. The Willmore energy is also scale-invariant, which means that it is preserved under rescaling of the surface, making it robust to changes in size or orientation.

(\mathcal{E}) Last, the Euler-Elastica-based energy is the key suggestion in our framework, being the third choice, which is the combination of two energies mentioned above

$$\mathcal{E}(E) = \mathcal{P}(E) + \mathcal{W}(E) = \int_{\partial E} (\mathbb{1}_E + |H|^2) d\mathcal{H}^{D-1} \quad (12)$$

with the indicator function $\mathbb{1}_E$ and the mean curvatures H on the boundary ∂E as (10) and (11). Clearly, the Euler-Elastica-based energy combines the perimeter-based energy and the Willmore-based energy, which makes it an effective energy functional for shape analysis and geometric modelling. The first indicator term measures the smoothness of the boundary, while the second term measures the curvature. By combining these two terms, the Euler-Elastica energy can capture both the local and global properties of a shape. Moreover, the Euler-Elastica energy has been shown to have desirable properties, such as convexity and stability, which makes it an attractive option for optimisation-based approaches.

Furthermore, in recent years, new formulations of these energies have been explored using the approaches of Γ -convergence and phase-field approximation. Notably, the Γ -convergence and phase-field approximation approaches have opened up new avenues for studying these energies and their properties, such as convergence, stability, and regularity. Moreover, the use of regularised functions in these formulations can be beneficial in numerical optimisation, as they allow for efficient computation of minimisers and can avoid issues associated with non-smooth functionals. These developments have led to significant progress in the field of geometric variational problems and their applications.

(\mathcal{P}_ε) Modica and Mortola in [9] along with additional literature [3, 10] revealed that the perimeter-based energy \mathcal{P} could be approximated using the classical phase-field formulation (Van der Waals-Cahn-Hilliard formulation, in accordance with other terminologies, say perimeter-based formulation \mathcal{P}_ε instead)

$$\mathcal{P}_\varepsilon(u) = \int_{\Omega} \left(\frac{\varepsilon}{2} |\nabla u|^2 + \frac{1}{\varepsilon} W(u) \right) d\Omega \quad (13)$$

where $W(u) = \frac{1}{2}u^2(1-u)^2$ and ε is the representative diffuse interface width. More specifically, the $\Gamma(L^1(\Omega))$ -limit is the Γ -convergence of \mathcal{P}_ε to the area functional as $\varepsilon \rightarrow 0$. In other words,

$$\Gamma(L^1(\Omega)) - \lim_{\varepsilon \rightarrow 0} \mathcal{P}_\varepsilon(u) = \mathcal{P}(u) = \int_{\Omega} d|\nabla u| \quad (14)$$

for $u \in \text{BV}(\Omega, \{0, 1\})$ where $u = 2\chi_{\Omega} - 1 = \mathbb{1}_{\Omega}$ with the characteristic function χ_{Ω} of the finite perimeter set Ω . Then, there exists $\mathcal{P}(u) = \int_{\Omega} d|\nabla u| = \mathcal{H}^{D-1}(\partial\Omega) = \int_{\partial\Omega} \mathbb{1}_{\Omega} d\mathcal{H}^{D-1}$.

(\mathcal{W}_ε) Further, they also demonstrated that the Willmore-based formulation \mathcal{W}_ε can be used to approximate (\rightsquigarrow) the Willmore-based energy \mathcal{W} [3, 9, 26], i.e.

$$\begin{aligned} \mathcal{W}(E) &= \int_{\partial E} |H|^2 d\mathcal{H}^{D-1} \\ \rightsquigarrow \mathcal{W}_\varepsilon(u) &= \frac{1}{2\varepsilon} \int_{\Omega} \left(\varepsilon \Delta u - \frac{1}{\varepsilon} W'(u) \right)^2 d\Omega \end{aligned} \quad (15)$$

where $W'(u) = u(u-1)(2u-1)$. Remark that $\mathcal{W}_\varepsilon(u)$ stands for the rescaled norm of L^2 -gradient flow of $\mathcal{P}_\varepsilon(u)$ [10].

(\mathcal{E}_ε) Eventually, we consider the Euler-Elastica-based formulation

$$\begin{aligned} \mathcal{E}_\varepsilon(u) &= \mathcal{P}_\varepsilon(u) + \mathcal{W}_\varepsilon(u) \\ &= \int_{\Omega} \left(\frac{\varepsilon}{2} |\nabla u|^2 + \frac{1}{\varepsilon} W(u) \right) d\Omega + \frac{1}{2\varepsilon} \int_{\Omega} \left(\varepsilon \Delta u - \frac{1}{\varepsilon} W'(u) \right)^2 d\Omega \end{aligned} \quad (16)$$

to approximate the Euler-Elastica-based energy where the double-well potential $W(u) = \frac{1}{2}u^2(1-u)^2$ has two minima and its first derivative is $W'(u) = u(u-1)(2u-1)$. Röger and Schätzle in [12], partially responding to the conjecture of De Giorgi [19], with additional literature [10, 11] proved that the approximation is established with respect to Γ -convergence of \mathcal{E}_ε

$$\Gamma(L^1(\Omega)) - \lim_{\varepsilon \rightarrow 0} \mathcal{E}_\varepsilon(u) = \int_{\partial\Omega} (\mathbb{1}_{\Omega} + |H_{\partial\Omega}|^2) d\mathcal{H}^{D-1} \quad (17)$$

where $\mathbb{1}_E$ is the indicator function, $H_{\partial\Omega}$ is the mean curvatures vector of $\partial\Omega$.

3. The New Model and its Numerical Algorithms. After establishing the necessary mathematical framework in Section 2, we propose a new model related to our objective functional (9), which utilises the Euler-Elastica-based formulation (16) by minimising

$$\begin{aligned} \mathcal{E}_\varepsilon(u) &= \int_\Omega \left(\frac{\varepsilon}{2} |\nabla u|^2 + \frac{1}{\varepsilon} W(u) \right) d\Omega + \frac{1}{2\varepsilon} \int_\Omega \left(\varepsilon \Delta u - \frac{1}{\varepsilon} W'(u) \right)^2 d\Omega \\ \text{s.t. } u_{E_0}^{in} &\leq u \leq u_{E_0}^{ex} \end{aligned} \quad (18)$$

subject to linear obstacle restrictions as (4) related to the initial set E_0 where the double-well potential $W(u) = \frac{1}{2}u^2(1-u)^2$ has two minima and its first derivative is $W'(u) = u(u-1)(2u-1)$.

3.1. Derivation for the Euler-Elastica-based Formulation. In the following, we derive the Euler-Lagrange (E-L) PDE for the Euler-Elastica-based formulation (16) in order to compute the (local) minimum of our model (18). For other two formulations (13) and (15), the derivation is analogous.

By Gâteaux derivative, for $\forall \tau$, there exists

$$\delta \mathcal{E} = \frac{1}{\varepsilon} \int_\Omega W'(u) \tau d\Omega + \varepsilon \int_\Omega \nabla u \cdot \nabla \tau d\Omega \quad (19a)$$

$$+ \varepsilon \int_\Omega \Delta u \cdot \Delta \tau d\Omega + \frac{1}{\varepsilon^3} \int_\Omega W'(u) \cdot W''(u) \tau d\Omega \quad (19b)$$

$$- \frac{1}{\varepsilon} \left(\int_\Omega \Delta \tau \cdot W'(u) d\Omega + \int_\Omega \Delta u \cdot W''(u) \tau d\Omega \right). \quad (19c)$$

Next by Green's formulae, for the second term of (19a), the first term of (19b) and of (19c), there exists

$$\int_\Omega \nabla u \cdot \nabla \tau d\Omega = \oint_\Gamma \nabla u \cdot \tau \cdot \mathbf{n} d\Gamma - \int_\Omega \Delta u \cdot \tau d\Omega, \quad (20)$$

$$\begin{aligned} \int_\Omega \Delta u \cdot \Delta \tau d\Omega &= \int_\Omega \Delta u \cdot \nabla \cdot \nabla \tau d\Omega = \oint_\Gamma \Delta u \cdot \nabla \tau \cdot \mathbf{n} d\Gamma - \int_\Omega \nabla \cdot (\Delta u) \cdot \nabla \tau d\Omega \\ &= \oint_\Gamma \Delta u \cdot \nabla \tau \cdot \mathbf{n} d\Gamma - \oint_\Gamma \nabla \cdot (\Delta u) \cdot \tau \cdot \mathbf{n} d\Gamma + \int_\Omega \Delta^2 u \cdot \tau d\Omega, \end{aligned} \quad (21)$$

and

$$\begin{aligned} \int_\Omega \Delta \tau \cdot W'(u) d\Omega &= \int_\Omega \nabla \cdot \nabla \tau \cdot W'(u) d\Omega \\ &= \oint_\Gamma \nabla \tau \cdot W'(u) \cdot \mathbf{n} d\Gamma - \int_\Omega \nabla \tau \cdot \nabla W'(u) d\Omega \\ &= \oint_\Gamma \nabla \tau \cdot W'(u) \cdot \mathbf{n} d\Gamma - \oint_\Gamma \tau \cdot \nabla W'(u) \cdot \mathbf{n} d\Gamma + \int_\Omega \tau \cdot \Delta W'(u) d\Omega. \end{aligned} \quad (22)$$

Therefore, assembling (19), (20), (21) and (22),

$$\begin{aligned}
\delta \mathcal{E} &= \frac{1}{\varepsilon} \int_{\Omega} W'(u) \tau \, d\Omega + \varepsilon \left(\oint_{\Gamma} \nabla u \cdot \tau \cdot \mathbf{n} \, d\Gamma - \int_{\Omega} \Delta u \cdot \tau \, d\Omega \right) \\
&\quad + \varepsilon \left(\oint_{\Gamma} \Delta u \cdot \nabla \tau \cdot \mathbf{n} \, d\Gamma - \oint_{\Gamma} \nabla \cdot (\Delta u) \cdot \tau \cdot \mathbf{n} \, d\Gamma + \int_{\Omega} \Delta^2 u \cdot \tau \, d\Omega \right) \\
&\quad + \frac{1}{\varepsilon^3} \int_{\Omega} W'(u) \cdot W''(u) \tau \, d\Omega \\
&\quad - \frac{1}{\varepsilon} \left(\oint_{\Gamma} \nabla \tau \cdot W'(u) \cdot \mathbf{n} \, d\Gamma - \oint_{\Gamma} \tau \cdot \nabla W'(u) \cdot \mathbf{n} \, d\Gamma \right. \\
&\quad \left. + \int_{\Omega} \tau \cdot \Delta W'(u) \, d\Omega + \int_{\Omega} \Delta u \cdot W''(u) \tau \, d\Omega \right) \\
&= \int_{\Omega} \left(\frac{1}{\varepsilon} W'(u) - \varepsilon \Delta u + \varepsilon \Delta^2 u + \frac{1}{\varepsilon^3} W'(u) \cdot W''(u) \right. \\
&\quad \left. - \frac{1}{\varepsilon} \Delta W'(u) - \frac{1}{\varepsilon} \Delta u \cdot W''(u) \right) \tau \, d\Omega + \oint_{\Gamma} \left(\varepsilon \Delta u \cdot \mathbf{n} - \frac{1}{\varepsilon} W'(u) \cdot \mathbf{n} \right) \nabla \tau \, d\Gamma \\
&\quad + \oint_{\Gamma} \left(\varepsilon \nabla u \cdot \mathbf{n} - \varepsilon \nabla \cdot (\Delta u) \cdot \mathbf{n} + \frac{1}{\varepsilon} \nabla W'(u) \cdot \mathbf{n} \right) \tau \, d\Gamma = 0
\end{aligned}$$

is permitted by the following E-L equation

$$\frac{1}{\varepsilon} W'(u) - \varepsilon \Delta u + \varepsilon \Delta^2 u + \frac{1}{\varepsilon^3} W'(u) \cdot W''(u) - \frac{1}{\varepsilon} \Delta W'(u) - \frac{1}{\varepsilon} \Delta u \cdot W''(u) = 0,$$

that is,

$$\frac{1}{\varepsilon} W'(u) - \varepsilon \Delta u + \Delta \left(\varepsilon \Delta u - \frac{1}{\varepsilon} W'(u) \right) - \frac{1}{\varepsilon^2} W''(u) \left(\varepsilon \Delta u - \frac{1}{\varepsilon} W'(u) \right) = 0. \quad (23)$$

3.2. Numerical Algorithm I. Following the above derivation of an E-L PDE, consider how to construct a numerical algorithm for our models with respect to \mathcal{E}_ε . A Cauchy problem is first recalled [3]

$$\begin{cases} u_t &= -\nabla \mathcal{E}_\varepsilon(u), \\ u(\xi, 0) &= u_0(\xi). \end{cases} \quad (24)$$

Here, \mathcal{E}_ε can be the perimeter-based \mathcal{P}_ε , Willmore-based \mathcal{W}_ε and Euler-Elastica-based \mathcal{E}_ε formulation, and $u_0(\xi)$ is from the initial set E_0 by (3). Then, by the Euler semi-implicit discretisation scheme in time [2], the approximate numerical scheme can be expressed with the presetting synthetic time step τ

$$\frac{u_{k+1} - u_k}{\tau} = -\nabla \mathcal{E}_\varepsilon(u_{k+1}). \quad (25)$$

In essence, the iterative solution u^{k+1} meets the regularisation with (9), that is,

$$u_{k+1} = \operatorname{argmin}_u \left\{ \frac{1}{2\tau} \int_{\Omega} (u - u_k)^2 \, d\Omega + \mathcal{E}_\varepsilon(u) \right\},$$

so that the restrictive conditions are promised as (4) aforesaid

$$\mathcal{E}_\varepsilon(u_{k+1}) \leq \frac{1}{2\tau} \int_{\Omega} (u_{k+1} - u_k)^2 \, d\Omega + \mathcal{E}_\varepsilon(u_{k+1}) \leq \mathcal{E}_\varepsilon(u_k).$$

In addition, we enforce the linear obstacle restriction (4) by applying the orthogonal projection to handle the inequality with increased relaxation, i.e.

$$u_{E_0}^{in} \leq u \leq u_{E_0}^{ex} \iff \max(\min(u, u_{E_0}^{ex}), u_{E_0}^{in}). \quad (26)$$

Accordingly, the numerical scheme of the E-L equation (23) for the Euler-Elastica-based formulation with respect to the time step τ is proposed as

$$u_t = \varepsilon \Delta u - \frac{1}{\varepsilon} W'(u) + \Delta \left(\frac{1}{\varepsilon} W'(u) - \varepsilon \Delta u \right) + \frac{1}{\varepsilon^2} W''(u) \left(\varepsilon \Delta u - \frac{1}{\varepsilon} W'(u) \right).$$

Following that, its numerical Euler semi-implicit discretisation scheme in time τ is expressed

$$\begin{aligned} \frac{u_{k+1} - u_k}{\tau} = & \varepsilon \Delta u_{k+1} - \frac{1}{\varepsilon} W'(u_{k+1}) + \Delta \left(\frac{1}{\varepsilon} W'(u_{k+1}) - \varepsilon \Delta u_{k+1} \right) \\ & + \frac{1}{\varepsilon^2} W''(u_{k+1}) \left(\varepsilon \Delta u_{k+1} - \frac{1}{\varepsilon} W'(u_{k+1}) \right). \end{aligned} \quad (27)$$

Clearly, reorganising above equation (27), there exists

$$\begin{aligned} u_{k+1} = & (I_D - \varepsilon \tau \Delta + \tau \varepsilon \Delta^2)^{-1} \\ & \left(u_k - \frac{\tau}{\varepsilon} W'(u_{k+1}) + \frac{\tau}{\varepsilon} \Delta W'(u_{k+1}) \right) \\ & - \frac{\tau}{\varepsilon} W''(u_{k+1}) \Delta u_{k+1} + \frac{\tau}{\varepsilon^3} W'(u_{k+1}) W''(u_{k+1}) \end{aligned} \quad (28)$$

that is, the point u_{k+1} is also a fixed point of the function

$$\begin{aligned} \Phi_{\mathcal{E}}(x) = & (I_D - \varepsilon \tau \Delta + \tau \varepsilon \Delta^2)^{-1} \\ & \left(u_k - \frac{\tau}{\varepsilon} W'(x) + \frac{\tau}{\varepsilon} \Delta W'(x) - \frac{\tau}{\varepsilon} W''(x) \Delta x + \frac{\tau}{\varepsilon^3} W'(x) W''(x) \right). \end{aligned} \quad (29)$$

Moreover, the prepositional operator of (29)

$$\rho_{\mathcal{E}}(\xi) = (I_D - \varepsilon \tau \Delta + \tau \varepsilon \Delta^2)^{-1} \quad (30)$$

is able to implement via fast Fourier transform (FFT) and its associated symbol of a differential operator

$$\rho_{\mathcal{E}}(\xi) = (I_D - \varepsilon \tau \Delta + \tau \varepsilon \Delta^2)^{-1} = \frac{1}{1 + 4\tau\varepsilon\pi^2|\xi|^2 + 16\tau\varepsilon\pi^4|\xi|^4}. \quad (31)$$

Overall, each iteration of the Projected Gradient Descent Method (PGDM) is summarised in the following Algorithm 3.1 for estimating the numerical solution of the Euler-Elastica-based formulation where another two options for perimeter-based formulation and Willmore-based formulation can be referred to [3].

3.3. Numerical Algorithm II. In recent years, there has been a lot of progress in developing fast alternating direction method of multipliers (ADMM) for various applications [22, 23]. Here we have extended the method to solve our model (18).

Expecting new variables $\mathbf{w} = \nabla u$ to have a faster numerical approximation, the formulation is converted to

$$\begin{aligned} \arg \min_{u, \mathbf{w}} \int_{\Omega} \left(\frac{\varepsilon}{2} |\mathbf{w}|^2 + \frac{1}{\varepsilon} W(u) \right) d\Omega + \frac{1}{2\varepsilon} \int_{\Omega} \left(\varepsilon \operatorname{div} \mathbf{w} - \frac{1}{\varepsilon} W'(u) \right)^2 d\Omega \\ \text{s.t. } \mathbf{w} = \nabla u \quad \text{and} \quad u_{E_0}^{in} \leq u \leq u_{E_0}^{ex}. \end{aligned} \quad (32)$$

Algorithm 3.1: Projected Gradient Descent Method (PGDM)**Input:** Initial set E_0 ; Parameters τ, ε .**Output:** Numerical solution u_{k+1} .

$$1 \text{ Initial input: } u_0 = q\left(\frac{d(\xi, E_0)}{\varepsilon}\right); \quad (3)$$

$$2 \text{ Interior restriction: } u_{E_0}^{in} = q\left(\frac{d(\xi, \Omega^{in})}{\varepsilon}\right); \quad (5)$$

$$3 \text{ Exterior restriction: } u_{E_0}^{ex} = 1 - q\left(\frac{d(\xi, \Omega^{ex})}{\varepsilon}\right); \quad (5)$$

4 **for** $k = 0, 1, \dots$ **do**

$$5 \quad \left. \begin{aligned} u_{k+\frac{1}{2}} &= \max(\min(u_k, u_{E_0}^{ex}), u_{E_0}^{in}); \\ u_{k+1} &= (I_D - \varepsilon\tau \Delta + \tau\varepsilon\Delta^2)^{-1} \end{aligned} \right\} \quad (26)$$

$$6 \quad \left. \begin{aligned} &\left(u_{k+\frac{1}{2}} - \frac{\tau}{\varepsilon} W'(u_{k+\frac{1}{2}}) + \frac{\tau}{\varepsilon} \Delta W'(u_{k+\frac{1}{2}}) \right. \\ &\quad \left. - \frac{\tau}{\varepsilon} W''(u_{k+\frac{1}{2}}) \Delta u_{k+\frac{1}{2}} + \frac{\tau}{\varepsilon^3} W'(u_{k+\frac{1}{2}}) W''(u_{k+\frac{1}{2}}) \right) \end{aligned} \right\}; \quad (28)$$

7 **End** till some stopping criteria are met.

Then, the augmented Lagrangian functional for the above is expressed as

$$\begin{aligned} \mathcal{L}^\rho(u, \mathbf{w}; \boldsymbol{\lambda}) &= \int_{\Omega} \left[\left(\frac{\varepsilon}{2} |\mathbf{w}|^2 + \frac{1}{\varepsilon} W(u) \right) + \frac{1}{2\varepsilon} \left(\varepsilon \operatorname{div} \mathbf{w} - \frac{1}{\varepsilon} W'(u) \right)^2 \right. \\ &\quad \left. + \langle \boldsymbol{\lambda}, \nabla u - \mathbf{w} \rangle + \frac{\rho}{2} |\nabla u - \mathbf{w}|^2 \right] d\Omega \\ &= \int_{\Omega} \left[\left(\frac{\varepsilon}{2} |\mathbf{w}|^2 + \frac{1}{\varepsilon} W(u) \right) + \frac{1}{2\varepsilon} \left(\varepsilon \operatorname{div} \mathbf{w} - \frac{1}{\varepsilon} W'(u) \right)^2 \right. \\ &\quad \left. + \frac{\rho}{2} |\nabla u - \mathbf{w} + \rho^{-1} \boldsymbol{\lambda}|^2 - \frac{\boldsymbol{\lambda}^2}{2\rho} \right] d\Omega \end{aligned} \quad (33)$$

with the penalty parameter $\rho > 0$ and the Lagrange multiplier $\boldsymbol{\lambda}$. Therefore, the problem in the ADMM can be considered as solving two subproblems and updating one multiplier:

$$\begin{cases} u_{k+1} = \arg \min_u \int_{\Omega} \left[\frac{1}{\varepsilon} W(u) - \frac{1}{\varepsilon} (\operatorname{div} \mathbf{w}_k) W'(u) + \frac{1}{2\varepsilon^3} (W'(u))^2 \right. \\ \quad \left. + \frac{\rho}{2} |\nabla u - \mathbf{w}_k + \rho^{-1} \boldsymbol{\lambda}_k|^2 \right] d\Omega \\ \mathbf{w}_{k+1} = \arg \min_{\mathbf{w}} \int_{\Omega} \left[\frac{\varepsilon}{2} |\mathbf{w}|^2 + \frac{\varepsilon}{2} (\operatorname{div} \mathbf{w})^2 - \frac{1}{\varepsilon} (\operatorname{div} \mathbf{w}) W'(u_{k+1}) \right. \\ \quad \left. + \frac{\rho}{2} |\mathbf{w} - \nabla u_{k+1} - \rho^{-1} \boldsymbol{\lambda}_k|^2 \right] d\Omega \\ \boldsymbol{\lambda}_{k+1} = \boldsymbol{\lambda}_k + \rho (\nabla u_{k+1} - \mathbf{w}_{k+1}) \end{cases} \quad (34)$$

For the u -subproblem of (34), by Gâteaux derivative, for $\forall \tau$, there exists

$$\delta \mathcal{E}_{u_{k+1}} = \int_{\Omega} \left(\frac{1}{\varepsilon} W'(u) \tau - \frac{1}{\varepsilon} \operatorname{div} \mathbf{w}_k W''(u) \tau + \frac{1}{\varepsilon^3} W'(u) W''(u) \tau \right) d\Omega \quad (35a)$$

$$+ \rho \int_{\Omega} (\nabla u - \mathbf{w}_k + \rho^{-1} \boldsymbol{\lambda}_k) \nabla \tau d\Omega. \quad (35b)$$

Next by Green's formulae, for (35b), there exists

$$\begin{aligned} & \int_{\Omega} (\nabla u - \mathbf{w}_k + \rho^{-1} \boldsymbol{\lambda}_k) \nabla \tau \, d\Omega \\ &= \oint_{\Gamma} (\nabla u - \mathbf{w}_k + \rho^{-1} \boldsymbol{\lambda}_k) \boldsymbol{\tau} \cdot \mathbf{n} \, d\Gamma - \int_{\Omega} \nabla \cdot (\nabla u - \mathbf{w}_k + \rho^{-1} \boldsymbol{\lambda}_k) \tau \, d\Omega. \end{aligned} \quad (36)$$

Therefore, assembling (35) and (36),

$$\begin{aligned} \delta \mathcal{E}_{u_{k+1}} &= \int_{\Omega} \left(\frac{1}{\varepsilon} W'(u) \tau - \frac{1}{\varepsilon} \operatorname{div} \mathbf{w}_k W''(u) \tau + \frac{1}{\varepsilon^3} W'(u) W''(u) \tau \right) \, d\Omega \\ &\quad + \rho \left(\oint_{\Gamma} (\nabla u - \mathbf{w}_k + \rho^{-1} \boldsymbol{\lambda}_k) \boldsymbol{\tau} \cdot \mathbf{n} \, d\Gamma \right. \\ &\quad \left. - \int_{\Omega} \nabla \cdot (\nabla u - \mathbf{w}_k + \rho^{-1} \boldsymbol{\lambda}_k) \tau \, d\Omega \right) = 0 \end{aligned}$$

is permitted by the following E-L equation

$$\frac{1}{\varepsilon} W'(u) - \frac{1}{\varepsilon} \operatorname{div} \mathbf{w}_k W''(u) + \frac{1}{\varepsilon^3} W'(u) W''(u) - \rho \nabla \cdot (\nabla u - \mathbf{w}_k + \rho^{-1} \boldsymbol{\lambda}_k) = 0. \quad (37)$$

Analogously, for the \mathbf{w} -subproblem of (34), by Gâteaux derivative, there exists

$$\begin{aligned} \delta \mathcal{E}_{\mathbf{w}_{k+1}} &= \int_{\Omega} \left(\varepsilon \mathbf{w} \boldsymbol{\tau} + \varepsilon \operatorname{div} \mathbf{w} \cdot \nabla \tau - \frac{1}{\varepsilon} W'(u_{k+1}) \Delta \mathbf{w} \cdot \boldsymbol{\tau} \right. \\ &\quad \left. + \rho (\mathbf{w} - \nabla u_{k+1} - \rho^{-1} \boldsymbol{\lambda}_k) \boldsymbol{\tau} \right) \, d\Omega \end{aligned} \quad (38)$$

for $\forall \boldsymbol{\tau}$. Next by Green's formulae, for the second term of (38), there exists

$$\int_{\Omega} \operatorname{div} \mathbf{w} \cdot \nabla \tau \, d\Omega = \oint_{\Gamma} \operatorname{div} \mathbf{w} \cdot \boldsymbol{\tau} \cdot \mathbf{n} \, d\Gamma - \int_{\Omega} \Delta \mathbf{w} \cdot \boldsymbol{\tau} \, d\Omega. \quad (39)$$

Therefore, assembling (38) and (39),

$$\begin{aligned} \delta \mathcal{E}_{\mathbf{w}_{k+1}} &= \int_{\Omega} \left(\varepsilon \mathbf{w} - \frac{1}{\varepsilon} W'(u_{k+1}) \Delta \mathbf{w} + \rho (\mathbf{w} - \nabla u_{k+1} - \rho^{-1} \boldsymbol{\lambda}_k) \right) \boldsymbol{\tau} \, d\Omega \\ &\quad + \varepsilon \left(\oint_{\Gamma} \operatorname{div} \mathbf{w} \cdot \boldsymbol{\tau} \cdot \mathbf{n} \, d\Gamma - \int_{\Omega} \Delta \mathbf{w} \cdot \boldsymbol{\tau} \, d\Omega \right) \end{aligned}$$

is permitted by the following E-L equation

$$\varepsilon \mathbf{w} - \frac{1}{\varepsilon} W'(u_{k+1}) \Delta \mathbf{w} + \rho (\mathbf{w} - \nabla u_{k+1} - \rho^{-1} \boldsymbol{\lambda}_k) - \varepsilon \Delta \mathbf{w} = 0. \quad (40)$$

Before proceeding with the numerical solutions, we first still enforce the linear obstacle restriction (4) as (26) in Algorithm 3.1 of Section 3.2, i.e.

$$u_{E0}^{in} \leq u \leq u_{E0}^{ex} \quad \iff \quad \max(\min(u, u_{E0}^{ex}), u_{E0}^{in}).$$

Then, to progress the numerical solution of (34), the minimising solution of u -subproblem is given by

$$\begin{aligned} \frac{u_{k+1} - u_k}{\tau} &= \rho \nabla \cdot (\nabla u_{k+1} - \mathbf{w}_k + \rho^{-1} \boldsymbol{\lambda}_k) - \frac{1}{\varepsilon} W'(u_{k+1}) \\ &\quad + \frac{1}{\varepsilon} \operatorname{div} \mathbf{w}_k W''(u_{k+1}) + \frac{1}{\varepsilon^3} W'(u_{k+1}) W''(u_{k+1}), \end{aligned} \quad (41)$$

which leads to the update

$$u_{k+1} = (I - \tau\rho\Delta)^{-1} \left[u_k + \tau \left(-\rho\nabla \cdot \mathbf{w}_k + \nabla \cdot \boldsymbol{\lambda}_k - \frac{1}{\varepsilon} W'(u_k) + \frac{1}{\varepsilon} \operatorname{div} \mathbf{w}_k W''(u_k) + \frac{1}{\varepsilon^3} W'(u_k) W''(u_k) \right) \right]. \quad (42)$$

Next, for the minimising solution of \mathbf{w} -subproblem, it is discretised by

$$\frac{\mathbf{w}_{k+1} - \mathbf{w}_k}{\tau} = \frac{1}{\varepsilon} W'(u_{k+1}) \Delta \mathbf{w}_{k+1} - \varepsilon \mathbf{w}_{k+1} + \rho (\mathbf{w}_{k+1} - \nabla u_{k+1} - \rho^{-1} \boldsymbol{\lambda}_k) + \varepsilon \Delta \mathbf{w}_{k+1}, \quad (43)$$

which issues in the update

$$\mathbf{w}_{k+1} = (I + \varepsilon\tau - \varepsilon\tau\Delta)^{-1} \left[\mathbf{w}_k + \frac{\tau}{\varepsilon} W'(u_{k+1}) \Delta \mathbf{w}_k + \tau\rho (\mathbf{w}_k - \nabla u_{k+1} - \rho^{-1} \boldsymbol{\lambda}_k) \right]. \quad (44)$$

Lastly, recall that the multiplier $\boldsymbol{\lambda}$ will be updated by

$$\boldsymbol{\lambda}_{k+1} = \boldsymbol{\lambda}_k + \rho (\nabla u_{k+1} - \mathbf{w}_{k+1}). \quad (45)$$

This completes one step of the ADMM method, with the final algorithm shown in Algorithm 3.2.

Algorithm 3.2: Alternating Direction Method of Multipliers (ADMM)

Input: Initial set E_0 ; Parameters τ, ε, ρ .

Output: Numerical solution u_{k+1} .

- 1 Initial input: $u_0 = q\left(\frac{d(\xi, E_0)}{\varepsilon}\right)$; (3)
 - 2 $\mathbf{w}_0 = \nabla u_0$;
 - 3 $\boldsymbol{\lambda}_0 = \mathbf{w}_0$;
 - 4 Interior restriction: $u_{E_0}^{in} = q\left(\frac{d(\xi, \Omega^{in})}{\varepsilon}\right)$; (5)
 - 5 Exterior restriction: $u_{E_0}^{ex} = 1 - q\left(\frac{d(\xi, \Omega^{ex})}{\varepsilon}\right)$; (5)
 - 6 **for** $k = 0, 1, \dots$ **do**
 - 7 $u_{k+\frac{1}{2}} = \max(\min(u_k, u_{E_0}^{ex}), u_{E_0}^{in})$; (26)
 - 8 $u_{k+1} = (I - \tau\rho\Delta)^{-1} \left[u_{k+\frac{1}{2}} + \tau (-\rho\nabla \cdot \mathbf{w}_k + \nabla \cdot \boldsymbol{\lambda}_k - \frac{1}{\varepsilon} W'(u_{k+\frac{1}{2}}) + \frac{1}{\varepsilon} \operatorname{div} \mathbf{w}_k W''(u_{k+\frac{1}{2}}) + \frac{1}{\varepsilon^3} W'(u_{k+\frac{1}{2}}) W''(u_{k+\frac{1}{2}})) \right]$; (42)
 - 9 $\mathbf{w}_{k+1} = (I + \varepsilon\tau - \varepsilon\tau\Delta)^{-1} \left[\mathbf{w}_k + \frac{\tau}{\varepsilon} W'(u_{k+1}) \Delta \mathbf{w}_k + \tau\rho (\mathbf{w}_k - \nabla u_{k+1} - \rho^{-1} \boldsymbol{\lambda}_k) \right]$; (44)
 - 10 $\boldsymbol{\lambda}_{k+1} = \boldsymbol{\lambda}_k + \rho (\nabla u_{k+1} - \mathbf{w}_{k+1})$; (45)
 - 11 **End** till some stopping criteria are met.
-

4. Experimental Results and Quantitative Comparisons with Analysis.

We are now ready to present some experimental results in this section. 3D reconstructed results will be performed in the following using

- 3D surface inpainting models extended from [15],
- the perimeter-based formulation (13),
- the Willmore-based formulation (15), and
- the new Euler-Elastica-based formulation (16),

where four inpainting models are tested as follows

- the Cahn-Hilliard model (see Section 5.3 in [15]),
- the Mumford-Shah model (see Chapter 7 in [15]),
- the transport model (see Section 6.1 in [15]), and
- the absolutely minimising Lipschitz extensions (see Section 4.4 in [15]).

The experimental results consist of two simulated examples, namely (**Example 1** Sphere like tumour-like simulation and **Example 2** Branching Cylinders as branching blood vessels mimicked), as well as two segmented realistic examples (**Example 3** Stent segmented from real CT images and **Example 4** Tumour segmented from real MRI images), and one realistic example (**Example 5** Deer from THz imaging). For **Example 1** Sphere, we demonstrate the simulation of the input slices and the gap-filling process (Figure 8). The results obtained using the compared models are presented in Figure 9 and Figure 10. However, only the inpainting results are shown in this example as they are unsatisfactory in meeting our expectations, despite some of them being feasible for gap filling (e.g. Figure 9(a) and (b)). In **Example 2** Branching Cylinders, we illustrate the feasibility of concave geometrical morphology for our formulations. The simulated input and its results using three formulations are depicted in Figure 11 and 12. To compare the results obtained from the three formulations and establish a benchmark as the stopping criterion, we propose an approach for **quantitative comparisons**. This is done through the mathematical and graphical interpretation (Equations (46)-(47) and Figure 13) from the perspective of discrete geometry. The variance of the two simulated examples is visualised in Figure 14 and 16 with histograms in Figure 15 and 17. Furthermore, the numeric corroboration of the comparison between the three formulations and **Examples 1-3** is presented in Table 1, and the **experimental convergence and computational complexity of PGDM for Example 1** is provided in Figure 18 and 19. Considering the gradient descent method used throughout ADMM, an **experimental analysis of ADMM for Example 1** is provided in Figure 20. This analysis focuses on the sensitivity of parameters to establish the relationship between the new formulation and parameters for faster and better numerical simulations. Lastly, we present the results of three realistic examples, (**Example 3** Stent segmented from real CT images, **Example 4** Tumour segmented from real MRI images, and **Example 5** Deer from THz imaging) in Figure 22-25. These results demonstrate the application of the new Euler-Elastica formulation and verify its merits. Remark that all implementations were coded using the computer programming language: MATLAB_R2022a[®] in the operating system: macOS Monterey (Version 12.5) equipped with a 2.3 GHz 8-Core Intel Core i9 Processor and 16GB 2667 MHz DDR4 Memory (some implementations in the revised version were carried out using MATLAB_R2023a[®] in the operating system: macOS Ventura (Version 13.3.1 (a)) equipped with an Apple M1 Max Chip and 64 GB Memory).

Example 1 (Sphere tested by all compared models). To simulate the reconstructed problem from a few slices, by setting the low resolution $N = 32$, the rough 5 slices are collected from a Sphere as tumour-like simulation being the first example as Figure 8(a) illustrated. Then, the initially rough surface can be straightforwardly constructed by duplicating the slices to fill the gaps as Figure 8(b) visualised. Remark that the gaps between the slices range from four to five. To fill the gap between the top and bottom slices, we duplicate half of the top slice and half of the bottom slice. For the remaining slices, we use the slices themselves to fill the half-up and half-down gaps.

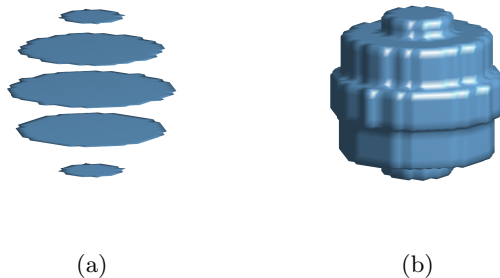


Figure 8. Visualisation of (b) the initial rough surface of **Example 1** Sphere by duplicating the slices from (a) the given 5 slices under the low resolution $N = 32$.

First, to compare the variational framework with phase-field approximation, we would like to demonstrate the results (see Figure 9) by the explored extension of four 3D surface inpainting models ((a) the Cahn-Hilliard model, (b) the Mumford-Shah model, (c) the transport model, and (d) the absolute minimising Lipschitz extensions) which are introduced from [15]. The extension from 2D image inpainting to 3D surface inpainting is explored by the case of missing slices in the vertical direction to restore one of the planes in two axes other than the vertical axis. Apparently, such a task is quite challenging for the above inpainting models, which these illustrated results are visually unacceptable with the time-consuming acquisition, and probably the sunken gaps would lead to unexpected variations even though the gaps of two of the results were filled. The main reason for unsatisfactory results by inpainting models is due to their local and partial inpainting without considering the global variation. Remark that the stopping criteria for each inpainting model are set as respectively: the maximum number 500 of iterations for the Cahn-Hilliard model; the residual less than the tolerance 10^{-14} for the Mumford-Shah model with the maximum number 50 of iterations; the residual less than the tolerance 10^{-5} for the transport model with the maximum number 50 of iterations; and the residual less than the tolerance 10^{-8} for the absolutely minimising Lipschitz extensions with the maximum number 50 of iterations.

Thereupon, for our variational framework with phase-field approximation, the parameters are set as $\varepsilon = 1.5/N$, $\tau = \varepsilon^4$, and the stopping criterion by the difference of corresponding energies between new iterative results and previous one less than the preset value. By the convergence results of (7), the surface by three formulations (perimeter-based, Willmore-based, and Euler-Elastica-based formulation) can be

extracted from the iterative results under the isosurface value at half as Figure 10 demonstrated. Under observation of Figure 10, the last one by investing the Euler-Elastica-based formulation is the desired result. Noted that applying the Willmore-based formulation produces a smoother surface with undesired shapes of the top and bottom due to achieving lower energy of mean curvature with the property of Willmore energy. Moreover, applying the perimeter-based formulation emerges small bulges patently, whereas it maintains the initial shape globally.

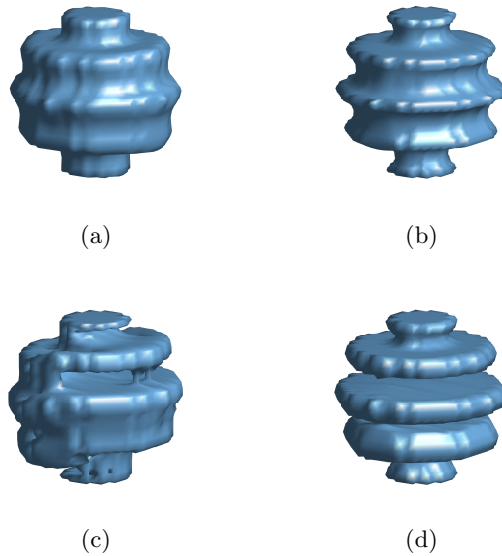


Figure 9. Inpainting results of **Example 1** Sphere by four models: (a) the Cahn-Hilliard model; (b) the Mumford-Shah model; (c) the transport model and (d) the absolute minimising Lipschitz extensions from Figure 8(a) the given 5 input slices under the low resolution $N = 32$. (Clearly, inpainting methods do not work well if given only a few slices.)

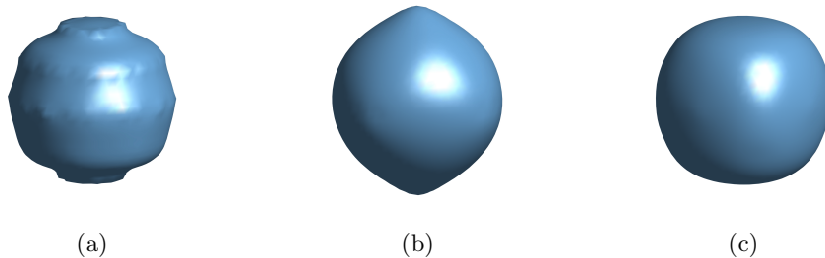


Figure 10. Final reconstructed results of **Example 1** Sphere by three formulations: (a) perimeter-based formulation; (b) Willmore-based formulation; and (c) Euler-Elastica-based formulation; from low-resolution inputs $N = 32$ with 5 slices. (Visually, the result (c) by the new model is the best.)

Example 2 (Branching Cylinders tested by three formulations). Analogously, for the second example: Branching Cylinders as branching blood vessels mimicked, Figure 11 delineates the initially rough surface under the same duplicating idea in the first example, which is constructed from the given 24 slices under the low resolution $N = 128$. Remark that the gap of collected slices is intentionally uneven so that the initial surface has a distinct fluctuation waiting to be restored, and the gap range is from three to thirteen.

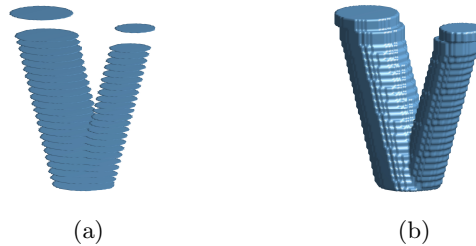


Figure 11. Visualisation of (b) the initial rough surface of **Example 2** Branching Cylinders from (a) the given 24 slices under the low resolution $N = 128$.

As the resolution of this example is increased, keeping the same diffuse interface width $\varepsilon = 1.5/N$ and setting the larger time step $\tau = \{\varepsilon^3, 10\varepsilon^4\}$ for the faster stable results where ε^3 for perimeter-based and Willmore-based formulation, and the latter one for Euler-Elastica-based formulation by the corresponding fixed point iterative schemes, then the reconstructed surfaces by three formulations are extracted as Figure 12 performed. Following the presupposition in Section 1, as the Euler-Elastica-based formulation merges the advantages of the perimeter-based formulation and the Willmore-based formulation to overcome the above deficiencies, the surface by the Euler-Elastica-based formulation is heralded the better reconstruction comparing by the Willmore-based formulation in this scenario either the top plane or the concave between the branching part.

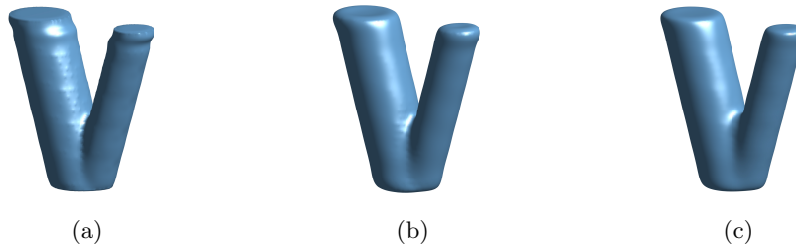


Figure 12. Final reconstructed results of **Example 2** Branching Cylinders by three formulations: (a) perimeter-based formulation; (b) Willmore-based formulation; and (c) Euler-Elastica-based formulation from low-resolution inputs $N = 128$ with 24 slices.

Quantitative Comparisons. Broadly speaking, the reconstruction of Branching Cylinders using the Willmore-based formulation (Figure 12(b)) initially fulfilled the initial requirements, exhibiting minor deficiencies that were difficult to discern through visual inspection alone. However, when compared to the results obtained using the newly proposed Euler-Elastica-based formulation, these deficiencies become more noticeable.

Accordingly, to indicate the level of smoothness for the above results by three formulations, the quantitative benchmark is considered by computing its standard deviation of Gaussian curvatures (GC) $\sigma_{GC} := \sigma(\kappa_G)$ and of mean curvatures (MC) $\sigma_{MC} := \sigma(\bar{\kappa})$ for surfaces represented by triangular meshes from the viewpoint of discrete geometry. To recap from the theoretical discrete geometry, the Gaussian curvature of each vertex is given by

$$\kappa_G(\mathbf{v}_i) = \frac{2\pi - \sum_{k=1}^{\mathbb{N}_{F_{iR}}} \theta_{i_k}}{\mathcal{A}_{iR}} \quad (46)$$

and the mean curvature of each vertex is given by

$$\bar{\kappa}(\mathbf{v}_i) = \frac{1}{2\mathcal{A}_{iR}} \sum_{j \in {}_R NV_i} (\cot \alpha_{ij} + \cot \beta_{ij})(\mathbf{v}_j - \mathbf{v}_i) \quad (47)$$

where \mathcal{A}_{iR} stands for the appropriately chosen area from the patch within R -ring neighbouring vertices ${}_R NV_i$ (i.e. the minimum number of edges from \mathbf{v}_i to the neighbouring vertex is less than or equal to R where, in this case, R is opted for 1) around the vertex \mathbf{v}_i , θ_{i_k} denotes the angle of the k^{th} face at the vertex \mathbf{v}_i , $\mathbb{N}_{F_{iR}}$ is the total number of faces in the set F_{iR} around this vertex \mathbf{v}_i , as well as α_{ij} and β_{ij} are two angles opposite to the sharing edge in the two triangles as Figure 13 exemplified, which can be consulted [20, 21] for more details. Remark that, by the concept of geometrical measure, the Gaussian curvature is intrinsically invariant and relies only on surface-estimated distances, yet the mean curvature embedded surface locally is extrinsic evaluation in some ambient space e.g. Euclidean space.

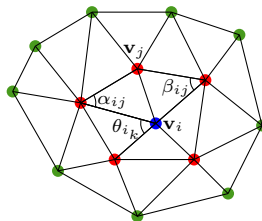


Figure 13. Computing curvatures – Illustration of the patch within the 2-ring neighbouring vertices ${}_2 NV_i$ of the centre vertex \mathbf{v}_i (blue) where the first ring neighbouring vertices are red, and the second ring neighbouring vertices are green.

In accordance with Figure 10 and Figure 12 for **Examples 1** and **2**, we present in Figure 14 and Figure 16 the variance of Gaussian curvature and mean curvature at each vertex of the triangular meshes, computed using three different formulations for these two examples. In order to facilitate the comparison of the results, we set the minimum (maximum) of the colorbar to the maximum (minimum) curvature of all

vertices for the three formulations and meshes: $\max(\min(\mathcal{P}), \min(\mathcal{W}), \min(\mathcal{E}))$ and $\min(\max(\mathcal{P}), \max(\mathcal{W}), \max(\mathcal{E}))$, respectively. We also provide histograms in Figure 15 and Figure 17 to show the proportional distribution of all curvatures at each vertex and to compare the curvature distributions across different meshes using three formulations. We note that, as expected for **Example 1** and **2** by \mathcal{E} , the majority of the curvatures cluster around zero.

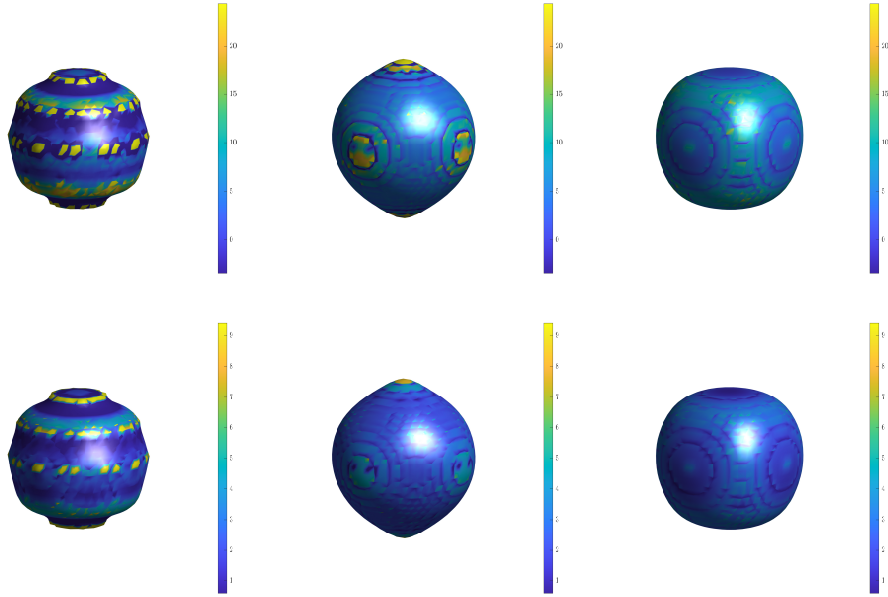


Figure 14. Visualisation of Gaussian curvatures (top line) and mean curvatures (bottom line) in final reconstructed results of **Example 1** Sphere by three formulations: perimeter-based formulation (left); Willmore-based formulation (middle); and Euler-Elastica-based formulation (right).

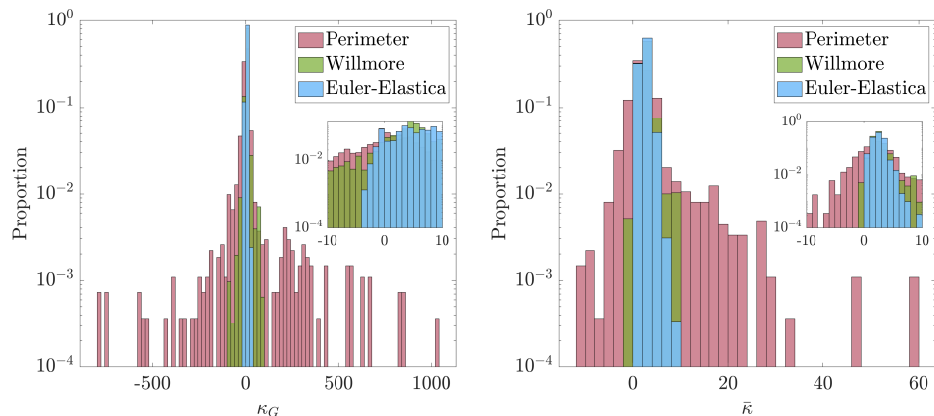


Figure 15. Histograms of all Gaussian curvatures κ_G (left) and mean curvatures $\bar{\kappa}$ (right) in final reconstructed results of **Example 1** Sphere by three formulations: perimeter-based formulation (pink); Willmore-based formulation (green); and Euler-Elastica-based formulation (cyan).

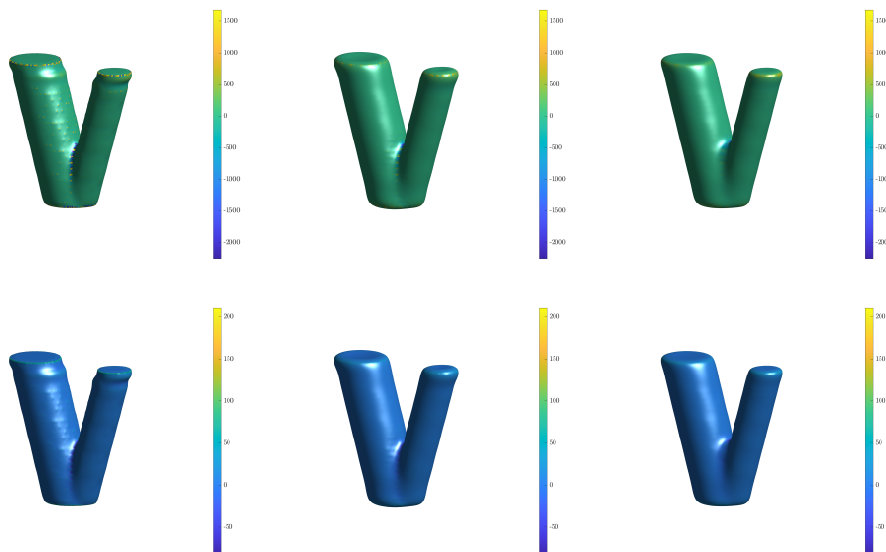


Figure 16. Visualisation of Gaussian curvatures (top line) and mean curvatures (bottom line) in final reconstructed results of **Example 2** Branching Cylinders by three formulations: perimeter-based formulation (left); Willmore-based formulation (middle); and Euler-Elastica-based formulation (right).

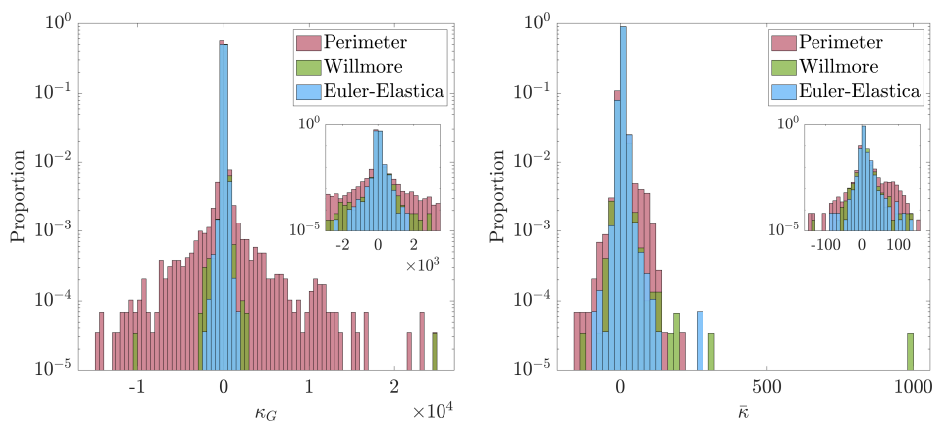


Figure 17. Histograms of all Gaussian curvatures κ_G (left) and mean curvatures $\bar{\kappa}$ (right) in final reconstructed results of **Example 2** Branching Cylinders by three formulations: perimeter-based formulation (pink); Willmore-based formulation (green); and Euler-Elastica-based formulation (cyan).

In Table 1, we present numerical comparisons of the three formulations for **Examples 1-3**, in terms of the standard deviation of Gaussian curvatures (σ_{GC}), the standard deviation of mean curvatures (σ_{MC}), and CPU elapsed time. We observe that, for the same input, the trend of values of σ_{GC} and σ_{MC} is decreasing, indicating that the level of smoothness is improving as the amount of variation is reduced, thus indicating a better reconstruction by the new proposed formulation. Additionally, we report the average elapsed time of each iteration by the three formulations, highlighting the computational efficiency of our numerical approach.

Table 1. Comparisons of the standard deviation of Gaussian curvatures σ_{GC} and of mean curvatures σ_{MC} , and of the average elapsed time of each iteration (seconds/iteration or s/iter) by three formulations: perimeter-based (\mathcal{P}), Willmore-based (\mathcal{W}), and Euler-Elastica-based (\mathcal{E}) formulation to three examples: **Example 1** (Figure 14), **Example 2** (Figure 16) and **Example 3** (Figure 22).

		Model \mathcal{P}	Model \mathcal{W}	New model \mathcal{E}
Example 1 Sphere ($N = 32$)	σ_{GC}	85.6522	10.5005	4.3289
	σ_{MC}	4.9897	1.2315	0.9789
	s/iter	0.0009	0.0030	0.0033
Example 2 Branching Cylinders ($N = 128$)	σ_{GC}	772.2918	191.8314	89.1912
	σ_{MC}	10.9077	8.9567	6.3708
	s/iter	0.0835	0.2791	0.3108
Example 3 Stent ($N = 512$)	σ_{GC}	16372.1718	1734.3918	1628.0449
	σ_{MC}	100.5420	35.2987	33.3259
	s/iter	0.4761	1.4679	1.4778

Experimental Convergence and Computational Complexity of PGDM for Example 1. To evaluate the convergence of the numerical algorithm I, in Figure 18, we plot the relative error between the current and previous iterations over the number of iterations for **Example 1** with respect to three formulations. From the convergence plot, we observe that the algorithm with Euler-Elastica-based formulation converges rapidly within the first 100 iterations and reaches a relative error of 10^{-4} after approximately 300 iterations.

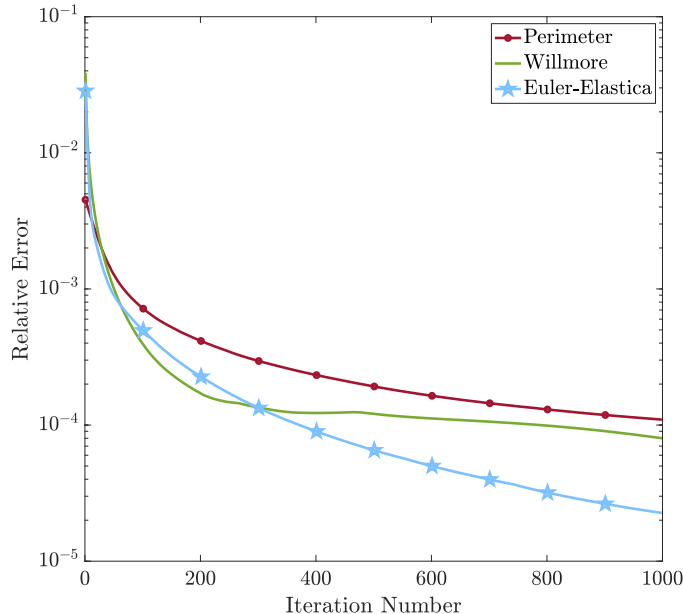


Figure 18. Experimental convergence curves by the relative error over the number of iterations for **Example 1** with respect to the perimeter-based (red with circles), the Willmore-based (green), and the Euler-Elastica-based (cyan with pentagrams) formulation.

Additionally, we evaluate the computational complexity of numerical algorithm I in terms of the number of iterations and the time required to run the algorithm. To estimate the computational complexity of an algorithm, we analyse the number of operations or steps the algorithm takes as the size N of the input increases. In our 3D scenario, the main operations inside the loop are the fast Fourier transform (FFT) and its inverse, which have a complexity of $\mathcal{O}(N \log N)$ for each axis. Besides, the Laplacian operator has a complexity of $\mathcal{O}(N^3)$, while the other operations have a lower complexity. Therefore, the computational complexity for each iteration of the algorithm I can be estimated as $\mathcal{O}(N^3 \log N)$. Here, we measured the running time for **Example 1** with various inputs N on the same hardware and software environment and used the unit of time set as the arbitrary unit (a.u.) in Figure 19. Then, we observe that the trend of experimental results and estimated arithmetical values are semblable. Note that the actual running time of an algorithm depends not only on its computational complexity but also on the specific hardware and software environment in which it is executed.

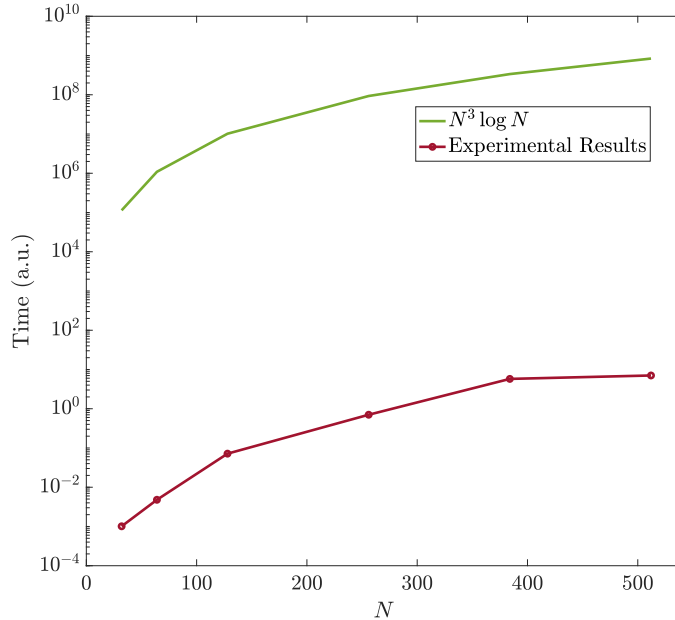


Figure 19. Computational complexity curves of experimental results (red with circles) and estimated arithmetical values (green) with various inputs N for **Example 1** where the unit of time is set as the arbitrary unit (a.u.).

Experimental Analysis of ADMM for Example 1. For the experimental results by the numerical algorithm II, the results are similar to the key computing gradient descent method used throughout ADMM. Meanwhile, the result by this algorithm is more sensitive than by the first Algorithm 3.1, which means the result is strongly influenced by the related parameters (the penalty parameter ρ , the diffuse interface width ε , and the time step τ), even though the speed of acquiring expected results is faster associated with fewer iterations.

Due to the sensitivity of parameters, Figure 20 provides the binary maps of testing in relation to the penalty parameter $\rho \in [0.5, 10]$ with the step of 0.5, and the representative diffuse interface width $\varepsilon \cdot N \in [1.5, 3]$ with the step of 0.1 for **Example 1** Sphere under the low resolution $N = 32$ in two time steps $\tau = \varepsilon^3$ and $\tau = \varepsilon^{3.5}$. After setting the criterion by our proposed benchmark in the case of the standard deviation of Gaussian curvatures σ_{GC} less than the value by the Willmore-based formulation which is $\sigma_{GC} < 10.5005$ in Table 1, then the binary maps can be ascertained the suitable range of parameters for the reliable results where the binary value 1 stands for the tolerable results existed, and 0 indicates the unpleasant results during the iterations.

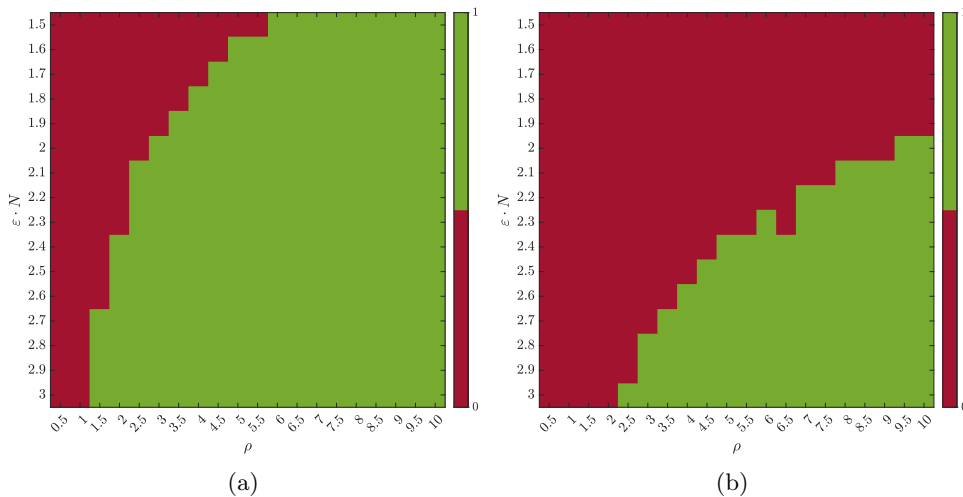


Figure 20. Binary maps of testing parameters sensitivity with respect to the penalty parameter $\rho \in [0.5, 10]$ with the step of 0.5 and the representative diffuse interface width $\varepsilon \cdot N \in [1.5, 3]$ with the step of 0.1 for **Example 1** Sphere under the low resolution $N = 32$ by the numerical algorithm II based on ADMM where 1 (green) stands for the tolerable results existed and 0 (red) indicates the unpleasant results during the iterations under the different time steps (a) $\tau = \varepsilon^3$ and (b) $\tau = \varepsilon^{3.5}$.

Example 3 (Stent segmented from real CT images). Last but not least, the realistic examples are procured from the variational segmentation work by Dr Liam Burrows [5] for the application of 3D reconstruction in medical imaging from 2D X-ray computed tomography (CT) scans and magnetic resonance imaging (MRI). Figure 21 visualises the direct construction by stacking all 48 2D low-resolution CT slices ($N = 512$) of the Chest. Then, the segmented Stent is constructed in the top line of Figure 22 and following the smoothed results by the Euler-Elastica-based formulation. Returning to the original objective of surface reconstruction from a reduced number of slices, Figure 23 demonstrates the efficacy of the new Euler-Elastica-based formulation by reconstructing the surface from only half of the available slices. This approach not only reduces the time required for data collection in clinical imaging, thereby minimising patient exposure to uncontrollable high-dose radiation, but also improves the quality of reconstructed objects by incorporating super-resolution techniques.

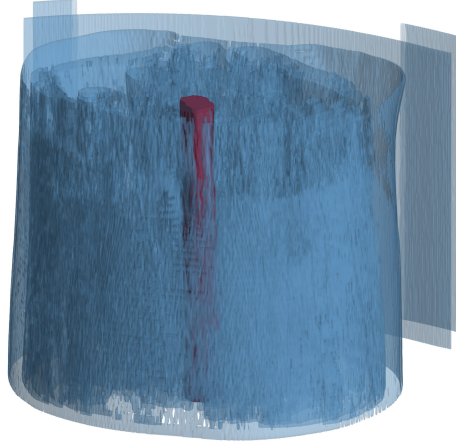


Figure 21. Visualisation of initial CT real data of the Chest (blue) under the low resolution $N = 512$ from 48 slices where **Example 3** segmented Stent is indicated as red.

Example 4 (Tumour segmented from real MRI images). In this example, we demonstrate the efficacy of our Euler-Elastica-based formulation in segmenting tumours from high-resolution MRI images. Specifically, we focus on a small region of interest in a large collection of 280 MRI images, resizing the area of interest to 150×150 pixels from the original size of 1210×2378 . This scenario poses a subtle challenge, as the small size of the region of interest makes it difficult to accurately segment the tumour from the surrounding tissue. However, by applying our new proposed model, we are able to achieve highly accurate results, as shown in Figure 24. Remark that we use the similar parameter settings as in **Example 3**, with the same time step of $\tau_t = \varepsilon^4$ and $\varepsilon = 2/N$ for the stent and $\varepsilon = 2.5/\bar{N}$ with the average pixel number \bar{N} of three axes for the tumour.

Example 5 (Deer from real THz imaging). Terahertz (THz) imaging has the potential to revolutionise medical imaging due to its non-ionising nature and ability to penetrate through certain materials. However, the images produced by THz imaging often suffer from low resolution with noise, and require significant time for acquisition [30]. The proposed Euler-Elastica-based formulation is also applicable for the 3D reconstruction from THz imaging data, as demonstrated by the example of a deer in Figure 25. By using the proposed formulation, we are able to effectively address the challenges posed by THz imaging and reconstruct smooth 3D models of the deer. The results, shown in Figure 25 (b), (d), (f), (h), illustrate the successful reconstruction from the full input of 218 slices (a) and fewer inputs (c), (e), (g). The parameter settings used for this example are $\tau = \varepsilon^{3.5}$ and $\varepsilon = 3/\max(N_x, N_y, N_z)$ with the maximum pixel number of three axes. These results demonstrate the potential of the proposed formulation for improving the quality and speeding up of 3D reconstructions from THz imaging data with low resolution and fewer slices, which can have important applications in medical imaging and other fields.

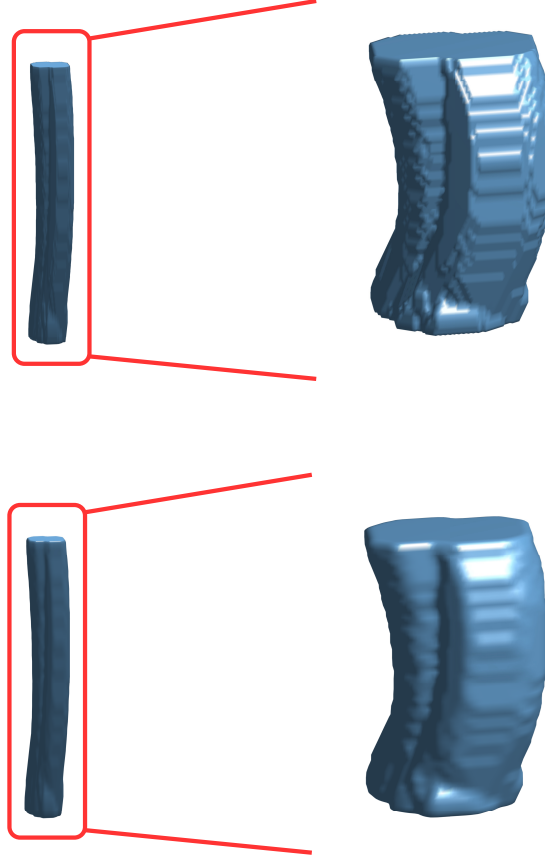


Figure 22. Visualisation of segmented rough input (top) of **Example 3** Stent from the given 48 slices of CT real data under the low resolution (Figure 21) and the smoothed reconstruction results by the Euler-Elastica-based formulation (bottom) where the results on the right column are the enlarged view of the left column.

5. **Conclusions.** The problem of reconstructing a high-quality 3D surface and achieving super-resolution is considered from a limited collection of low-resolution 2D slices. We proposed an Euler-Elastica-based formulation in the phase-field framework, which allows for improved construction quality by capturing both local edge features and global surface smoothness. Two numerical algorithms are developed for the numerical implementations. Besides visual comparisons with existing methods, we have compared construction qualities by measuring Gaussian curvatures and mean curvatures, showing that the proposed model outperforms previous works. The presented findings validate the effectiveness of addressing the challenges and offer promising prospects for various applications in medical imaging, computer vision, and other fields where high-quality surface reconstruction is essential.

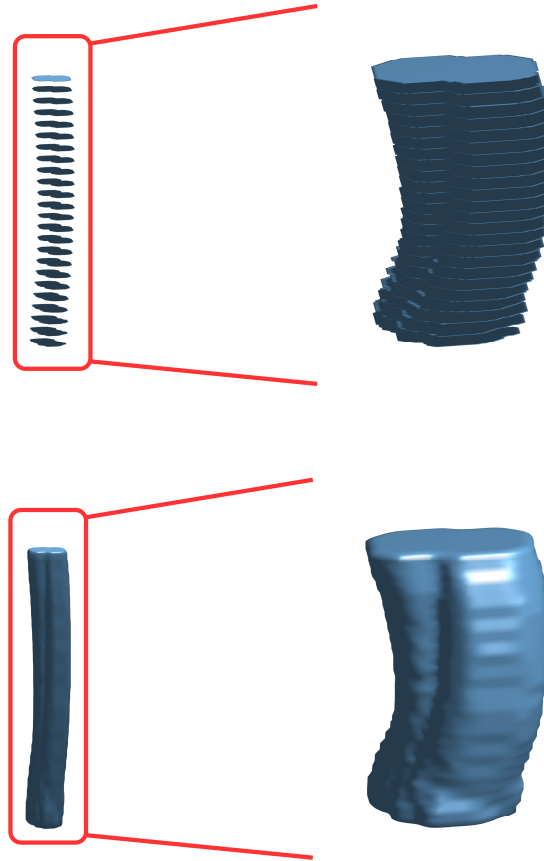


Figure 23. Visualisation of segmented rough input slices (top) of **Example 3** Stent by less 24 slices from CT real data under the low resolution (Figure 21) and the smoothed reconstruction results by the Euler-Elastica-based formulation (bottom) where the results on the right column are the enlarged view of the left column.

Acknowledgments. All authors would like to express their sincerest gratitude for the time and effort all referees and editors have dedicated to improving the quality of our work. The first author is grateful for partial support from the UoL-NTHU Dual PhD Programme and would like to express particular appreciation to Dr Elie Bretin for the clear explanations and implementations of their work in publications, as well as to Dr Liam Burrows for sharing his segmented real data. S.-H. Yang expresses thanks for the support from the Ministry of Science and Technology, Taiwan (MOST 110-2636-E-007-017).



Figure 24. Visualisation of segmented rough input (left) of **Example 4** Tumour from the given 280 slices of MRI real data and the smoothed reconstruction results by the Euler-Elastica-based formulation (right).

REFERENCES

- [1] N. Amenta and M. Bern, [Surface reconstruction by Voronoi filtering](#), *Discrete & Computational Geometry. An International Journal of Mathematics and Computer Science*, **22**(4) (1999), 481–504.
- [2] R. Backofen, M. Salvalaglio, A. Voigt and S. M. Wise, [Convexity splitting in a phase field model for surface diffusion](#), *International Journal of Numerical Analysis and Modeling*, **16**(2) (2019), 192–209. Available from: https://www.global-sci.org/intro/article_detail/ijnam/12799.html.
- [3] E. Bretin, F. Dayrens and S. Masnou, [Volume reconstruction from slices](#), *SIAM Journal on Imaging Sciences*, **10**(4) (2017), 2326–2358.
- [4] C. Brito-Loeza and K. Chen, [Fast iterative algorithms for solving the minimization of curvature-related functionals in surface fairing](#), *International Journal of Computer Mathematics*, Taylor & Francis, **90**(1) (2013), 92–108.
- [5] L. Burrows, W. Guo, K. Chen and F. Torella, [Reproducible kernel Hilbert space based global and local image segmentation](#), *Inverse Problems and Imaging*, **15**(1) (2021), 1–25.
- [6] T. Chan and W. Zhu, [Level set based shape prior segmentation](#), *CVPR 2005: IEEE Computer Society Conference on Computer Vision and Pattern Recognition*, (2005), 1164–1170.
- [7] F. Evrard, F. Denner and B. van Wachem, [Surface Reconstruction from Discrete Indicator Functions](#), *IEEE Transactions on Visualization and Computer Graphics*, **25**(3), (2019), 1629–2626.
- [8] M. Kazhdan and H. Hoppe, [Screened poisson surface reconstruction](#), *ACM Transactions on Graphics (TOG)*, **32**(3), (2013), 1–13.
- [9] L. Modica and S. Mortola, Il limite nella Gamma-convergenza di una famiglia di funzionali ellittici, *Bollettino della Unione Matematica Italiana. Series V. A*, **14**, (1977), 285–299.
- [10] L. Mugnai, [Gamma-convergence results for phase-field approximations of the 2D-Euler Elastica Functional](#), *ESAIM - Control, Optimisation and Calculus of Variations*, **19**(3), (2013), 740–753.
- [11] Y. Nagase and Y. Tonegawa, [A singular perturbation problem with integral curvature bound](#), *Hiroshima Mathematical Journal*, **37**(3), (2007), 455–490.
- [12] M. Röger and R. Schätzle, [On a Modified Conjecture of De Giorgi](#), *Mathematische Zeitschrift*, **254**(4), (2006), 675–714.
- [13] J. A. Sethian, [A Fast Marching Level Set Method for Monotonically Advancing Fronts](#), *Proceedings of the National Academy of Sciences of the United States of America*, **93**(4), (1996), 1591–1595.
- [14] H. Anton and C. Rorres, *Elementary linear algebra: with supplemental applications*, Wiley, 2011.

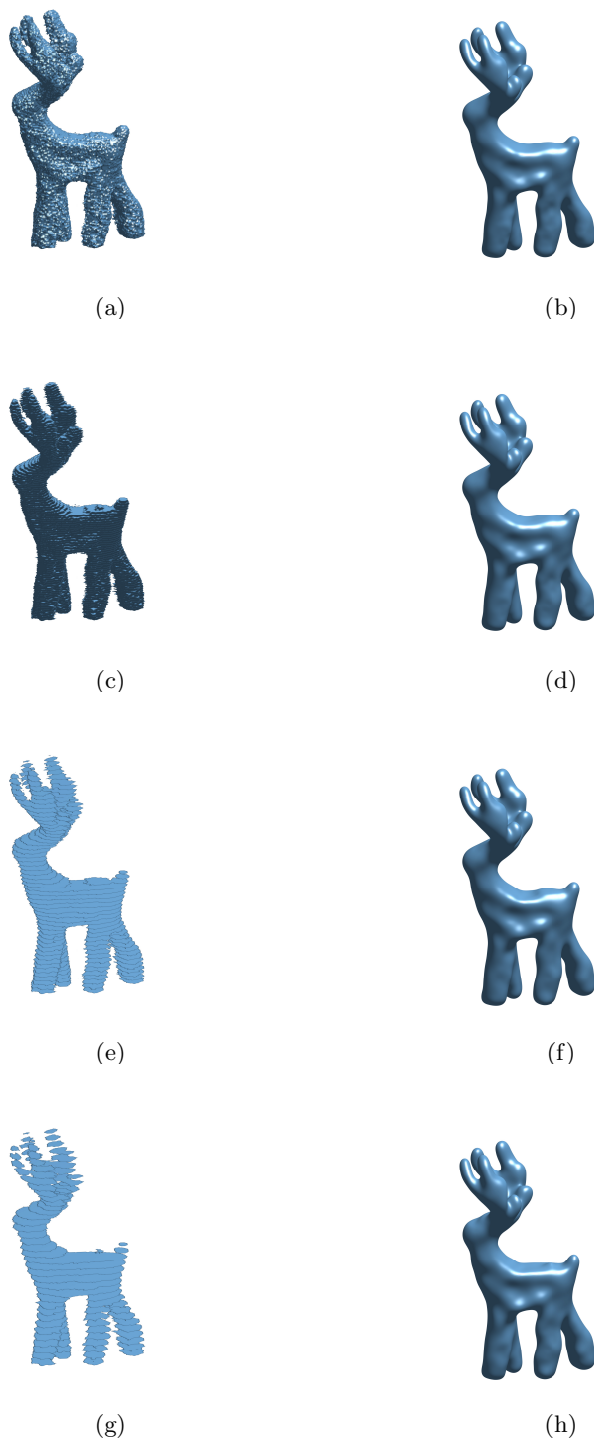


Figure 25. Visualisation of **Example 5** Deer from THz imaging: (a) rough input with noise from the given all 218 slices; (b) smoothed reconstruction result by the Euler-Elastica-based formulation from (a); (c) input 109 slices with 1 gap; (d) output from (c); (e) input 55 slices with 3 gaps; (f) output from (e); (g) input 37 slices with 5 gaps; (h) output from (g).

Appendix A. Summary of Notations.

Notations	Implications
D	Dimension of the space.
\mathbb{R}^D	D -dimensional Euclidean space.
$\tilde{E} (E_0)$	Target (Initial) set.
$E^* (E)$	Final (Potential) result.
$\{\Pi_s\}$	Set of the given s parallel cross-sections/slices/hyperplanes Π_s .
$\omega^{in} (\omega^{ex})$	Set of the interior (exterior) restriction $\omega_s^{in} (\omega_s^{ex})$ for all slices.
$\Omega^{in} (\Omega^{ex})$	Set of the fattened interior (exterior) restriction $\bigcup_s \Omega_{s,h}^{in} (\bigcup_s \Omega_{s,h}^{ex})$ for all slices with the thickness h .
$d_s(\xi, \pi_s)$	Signed distance function (oriented distance function) that identifies the distance between the given point ξ to an arbitrary subset π_s of hyperplanes Π_s .
$q(\cdot)$	Profile function.
$W(\cdot)$	Double-well potential function.
$u_\varepsilon(\cdot)$	Phase-field function.
$u_{E_0}^{in} := u_\varepsilon^{in}$ $(u_{E_0}^{ex} := u_\varepsilon^{ex})$	Phase-field profiles/approximations of the interior (exterior) restriction $\Omega^{in} (\Omega^{ex})$ with the thickness control $\varepsilon > 0$ for $h = \varepsilon^\alpha$.
$\mathbb{1}_\Omega(\chi_\Omega)$	Indicator function (characteristic function) of set Ω .
\mathcal{H}^D	D -dimensional Hausdorff measure.
H	Mean curvatures.
$\mathcal{E} = \mathcal{P}, \mathcal{W}, \mathcal{E}$	Variational energy, which can be the Perimeter-based \mathcal{P} , the Willmore-based \mathcal{W} , or the Euler-Elastica-based \mathcal{E} energy.
$\mathcal{P}_\varepsilon, \mathcal{W}_\varepsilon, \mathcal{E}_\varepsilon$	Perimeter-based formulation, Willmore-based formulation, Euler- Elastica-based formulation.
$\Gamma - \lim$	Γ -convergence.
τ	Synthetic time step.
ρ	Penalty parameter.
∇u	Gradient operator: $\nabla u = \left(\frac{\partial u}{\partial \xi_1}, \dots, \frac{\partial u}{\partial \xi_D} \right)$.
$\operatorname{div} u$	Divergence operator: $\operatorname{div} u = \sum_{i=1}^D \frac{\partial u}{\partial \xi_i}$.
Δu	Laplacian operator: $\Delta u = \sum_{i=1}^D \frac{\partial^2 u}{\partial \xi_i^2}$.
$\sigma_{GC} := \sigma(\kappa_G)$ $(\sigma_{MC} := \sigma(\bar{\kappa}))$	Standard deviation of Gaussian (mean) curvatures.

- [15] C.-B. Schönlieb, *Partial Differential Equation Methods for Image Inpainting*, Cambridge University Press, 2015.
- [16] G. Aubert and P. Kornprobst, *Mathematical problems in image processing: partial differential equations and the calculus of variations*, New York: Springer, 2006.
- [17] T. F. Chan and J. Shen, *Image processing and analysis: variational, PDE, wavelet, and stochastic methods*, Society for Industrial and Applied Mathematics, 2005.
- [18] F. Cazals and J. Giesen, Delaunay Triangulation Based Surface Reconstruction, in *Effective Computational Geometry for Curves and Surfaces*, Springer Berlin Heidelberg, 2006, 231–276.
- [19] E. De Giorgi, Some remarks on Γ -convergence and least squares method, in *Composite Media and Homogenization Theory: An International Centre for Theoretical Physics Workshop Trieste, Italy, January 1990*, Birkhäuser Boston, 1991, 135–142.
- [20] M. Meyer, M. Desbrun, P. Schröder and A. H. Barr, Discrete Differential-Geometry Operators for Triangulated 2-Manifolds, in *Visualization and Mathematics III*, Springer Berlin Heidelberg, 2003, 35–57. Available from: https://link.springer.com/chapter/10.1007/978-3-662-05105-4_2.
- [21] J. Wang and Z. Yu, A Novel Method for Surface Mesh Smoothing: Applications in Biomedical Modeling, in *Proceedings of the 18th International Meshing Roundtable*, Springer Berlin Heidelberg, 2009, 195–210. Available from: https://link.springer.com/chapter/10.1007/978-3-642-04319-2_12.
- [22] X.-C. Tai, J. Hahn and G. J. Chung, A Fast Algorithm for Euler’s Elastica Model Using Augmented Lagrangian Method, *SIAM Journal on Imaging Sciences*, **4**(1) (2011), 313–344.
- [23] M. Yashtini and S. H. Kang, Alternating Direction Method of Multiplier for Euler’s Elastica-Based Denoising, *Scale Space and Variational Methods in Computer Vision*, Lecture Notes in Computer Science, 9087, Springer, Cham, 2015, 690–701.
- [24] P. Alliez, D. Cohen-Steiner, Y. Tong and M. Desbrun, Voronoi-based variational reconstruction of unoriented point sets, *Proceedings of the fifth Eurographics symposium on Geometry processing*, 2007, 39–48.
- [25] N. Amenta, M. Bern and M. Kamvysselis, A new Voronoi-based surface reconstruction algorithm, *Proceedings of the 25th annual conference on Computer graphics and interactive techniques*, 1998, 415–421.
- [26] E. Bretin, Approximation par champ de phase de mouvement par courbure moyenne anisotrope, *Rencontre du PPF Dysco 2009*, 2009. Available from: <https://hal.archives-ouvertes.fr/hal-00750548>.
- [27] J. C. Carr, R. K. Beatson, J. B. Cherrie, T. J. Mitchell, W. R. Fright, B. C. McCallum and T. R. Evans, Reconstruction and representation of 3D objects with radial basis functions, *Proceedings of the 28th annual conference on Computer graphics and interactive techniques*, 2001, 67–76.
- [28] H.-K. Zhao, S. Osher and R. Fedkiw, Fast surface reconstruction using the level set method, *Proceedings IEEE Workshop on Variational and Level Set Methods in Computer Vision*, 2001, 194–201.
- [29] M. Kazhdan, M. Bolitho and H. Hoppe, Poisson surface reconstruction, *Proceedings of the fourth Eurographics symposium on Geometry processing*, 2006, 61–70.
- [30] Y. Zhang, K. Chen and S.-H. Yang, Fast Terahertz 3D Super-Resolution Surface Reconstruction by Variational Model from Limited Low-Resolution Sampling, *2022 47th International Conference on Infrared, Millimeter and Terahertz Waves (IRMMW-THz)*, Delft, Netherlands, 2022, 1–2.

Received xxxx 20xx; revised xxxx 20xx; early access xxxx 20xx.

E-mail address: Yiyao.Zhang@liverpool.ac.uk; yiyaozhang@gapp.nthu.edu.tw

E-mail address: K.Chen@strath.ac.uk

E-mail address: shanghua@ee.nthu.edu.tw